Journal of Neuroinflammation

RESEARCH

Open Access

Lactate accumulation from HIF-1α-mediated PMN-MDSC glycolysis restricts brain injury after acute hypoxia in neonates

Xiaogang Zhang[1,2†], Laiqin Peng[3†], Shuyi Kuang[2†], Tianci Wang[2†], Weibin Wu[4†], Shaowen Zuo[2], Chunling Chen[5], Jiaxiu Ye[3], Guilang Zheng[5*], Yuxiong Guo[5*] and Yumei He[1,2*]

Abstract

Fetal intrauterine distress (FD) during delivery can cause fetal intrauterine hypoxia, posing significant risks to the fetus, mother, and newborns. While studies highlight the role of polymorphonuclear myeloid-derived suppressor cells (PMN-MDSCs) in neonatal diseases and tumor hypoxia, their specific involvement in newborns experiencing fetal distress during delivery (FDNB) is not well understood. Here, we found elevated PMN-MDSC activation, increased glycolysis, enhanced lactate production, and upregulated HIF-1α expression in the blood of FDNB neonates compared to healthy newborns (NNB). Importantly, PMN-MDSC levels were inversely correlated with neuron-specific enolase (NSE), a marker for neurological injury. In neonatal mice subjected to acute hypoxia, a 48-h exposure led to a shift from exacerbation to amelioration of brain damage when compared with a 24-h period. This change was associated with a reduction in microglial activation, a decrease in the expression of inflammatory factors within the microglia, alongside increased peripheral PMN-MDSC activation. Depleting PMN-MDSCs led to heightened microglial activation and aggravated brain injury. Mechanistically, enhanced activation of PMN-MDSCs promotes HIF-1α accumulation while enhancing glycolysis and lactate release, thereby mitigating neonatal brain injury. Notably, lactate supplementation in hypoxic mice rescued brain damage caused by insufficient PMN-MDSC activation due to HIF-1α deficiency. Our study clarifies the role of lactate in peripheral PMN-MDSCs after acute hypoxia and its effects on microglial activation and subsequent brain injury.

Keywords Fetal intrauterine distress, Polymorphonuclear myeloid-derived suppressor cells, HIF-1α, Glycolysis, Lactate, Microglial activation, Inflammatory factors expression

†Xiaogang Zhang, Laiqin Peng, Shuyi Kuang, Tianci Wang and Weibin Wu contributed equally to this work.

*Correspondence:
Guilang Zheng
zhengguilang@gdph.org.cn
Yuxiong Guo
guoyuxiong@gdph.org.cn
Yumei He
hym0909@smu.edu.cn
[1]Pediatric Intensive Care Unit, Guangdong Provincial People's Hospital (Guangdong Academy of Medical Sciences), Department of Immunology, School of Basic Medical Sciences, Southern Medical University, Guangzhou, China
[2]Department of Immunology, Guangdong Provincial Key Laboratory of Single Cell Technology and Application, School of Basic Medical Sciences, Southern Medical University, Guangzhou, China
[3]Department of Gynecology and Obstetrics, Huizhou Central People's Hospital, Huizhou, China
[4]Department of Neonatology, Nanfang Hospital, Southern Medical University, Guangzhou, China
[5]Pediatric Intensive Care Unit, Guangdong Provincial People's Hospital (Guangdong Academy of Medical Sciences), Southern Medical University; Guangdong Provincial Cardiovascular Institute, Guangdong Provincial People's Hospital, Guangdong Academy of Medical Sciences,, Guangzhou, China

Introduction

Common prenatal abnormalities during childbirth include umbilical cord entanglement, placenta previa, and fetal distress. Intrauterine fetal distress (FD) often stems from hypoxia or inadequate oxygen supply, leading to potential brain damage and cerebral palsy in newborns, significantly impacting neonatal disability and mortality rates [1, 2]. It also contributes to neonatal hypoxia-ischemic encephalopathy (HIE) [3]. Acute hypothermia therapy is the primary clinical intervention for HIE; however, neurological damage and mortality can still occur post-treatment [4, 5]. Interventions such as nanoparticle hemoglobin vesicle delivery and artesian treatment have offered partial relief from FD [6], but their efficacy in preventing or treating secondary brain injuries resulting from intrauterine fetal distress in newborns (FDNB) remains uncertain. The incidence of advanced maternal age (AMA) has risen significantly due to increased education and advancements in assisted reproductive technologies. This trend is especially notable after the introduction of universal two- and three-child policies [7, 8]. Additionally, AMA is linked to a higher incidence of fetal distress [9]. Hence, inhibiting neuroinflammation as a pivotal approach to prevent HIE by regulating FDNB-induced brain injury has piqued the interest of researchers.

Microglia, the main immune cells of the central nervous system (CNS), and monocyte-derived macrophages (MDMs) from peripheral circulation play crucial roles in brain injury, repair, and inflammation regulation across various CNS diseases [10–12]. Research highlights differences in CD45 expression that help distinguish microglia ($CD11b^{+}CD45^{low}$) from macrophages ($CD11b^{+}CD45^{high}$) [13]. Additionally, microglia are activated in response to brain injury and immune stimulation, as evidenced by the expression of calcium-binding regulatory protein 1 (IBA-1) and cluster of differentiation 68 (CD68) within the hippocampal region [11, 14–17]. Recently, activated microglia were found to exhibit a $CD11b^{+}CD45^{high}$ phenotype under pathological conditions [18]. Notably, activated microglia and macrophages expressed inflammation-related markers, including pro-inflammatory markers like CD80, and CD86, as well as the anti-inflammatory marker CD206 [16, 19]. And both cells are regulated by the signal transducer and activator of transcription 1 (STAT1) and nuclear factor-kappa B (NF-κB) signal pathways. Emerging evidence indicates that the expression of inflammation-associated markers in these cells is closely linked to neuroinflammation [13, 20–22]. Microglia and macrophages from rat lesions treated with 6-OHDA showed an increase in $CD206^{+}$ cells and a decrease in $CD80^{+}$ or $CD86^{+}$ cells, along with inflammation remission [23]. In neonatal hypoxic-ischemic brain injury models, the upregulation of the anti-inflammatory marker CD206 is associated with reduced pro-inflammatory responses in microglia and macrophages [3]. Besides, $CD80^{+}$ or $CD86^{+}$ cells are immunostimulatory myeloid cells, including myeloid-derived suppressor cells (MDSCs), which help resolve systemic neuroinflammation [23]. Recent studies have implicated MDSCs in protecting against inflammatory damage in neonatal infectious diseases [24, 25]. Increased MDSC activity during infections may enhance neonatal resistance to bacterial infections such as septicemia [26]. However, the specific roles of microglia, macrophages, and MDSCs in FDNB and brain damage remain unexplored.

The hypoxia-inducible factor (HIF) family, including HIF-1α, HIF-2α, and HIF-1β, plays a crucial role in various diseases under hypoxic conditions. HIF-1α is particularly noted for its neuroprotective effects in neonatal hypoxic ischemic brain damage (HIBD) [27–30]. Activating the HIF-1α/VEGF pathway in rat models decreases infarct size and improves neurological function [28], indicating its potential therapeutic applications for neonatal brain injury [31–34]. Conversely, research highlights HIF-1α's role as a transcription factor in MDSCs within tumors, affecting metabolic reprogramming [35–40]. Liu et al. have identified the importance of the SIRT1-mTOR/HIF-1α glycolytic pathway in MDSC differentiation, providing insights into cancer therapies [35]. Furthermore, HIF-1α-related glycolysis influences MDSC function in liver diseases [37] and enhances anti-inflammatory activity in PMN-MDSCs during *Staphylococcus aureus* prosthetic joint infections [38, 41]. Notably, inhibiting HIF-1α and its glycolytic activity increases MDSC immunosuppression [42]. However, precise roles of MDSCs in FDNB and their neuroprotective mechanisms involving HIF-1α remain unclear.

We demonstrate that HIF-1α-mediated glycolysis in PMN-MDSCs is crucial for neonatal brain injury after acute hypoxia. Clinical findings show increased activation of PMN-MDSCs in the peripheral blood of FDNB compared to NNB, correlating with heightened anti-inflammatory signals and a negative correlation with neuron-specific enolase (NSE) levels. Furthermore, PMN-MDSCs from FDNB exhibit elevated levels of HIF-1α, glycolysis, and lactate. Animal model studies demonstrate that activated PMN-MDSCs play a crucial role in mitigating post-hypoxia brain damage in neonatal mice by modulating microglial activation and inflammatory factor expression in a time-dependent manner. Conditional knockout of HIF-1α confirms its critical role in activating PMN-MDSCs under hypoxia. Enhanced activation of PMN-MDSCs leads to increased levels of HIF-1α, glycolysis, and lactate, thereby mitigating neonatal brain injury. Lactate supplementation in hypoxic mice reduces brain damage caused by insufficient PMN-MDSC activation due to HIF-1α deficiency.

Our findings provide new insights into neonatal brain injury research by emphasizing the role of lactate as a glycolytic product of peripheral PMN-MDSCs.

Methods

Human samples

Peripheral blood samples were collected from two groups: healthy newborns with normal delivery (NNB) and newborns with fetal distress during delivery (FDNB). The samples were obtained from the Guangdong Provincial People's Hospital and the Nanfang Hospital of Southern Medical University, in Guangzhou, China. The samples were analyzed within 2 h of collection. The collection period spanned January 2021 to November 2024, and the samples were taken from newborns within 0–1 days of birth. To ensure homogeneity of the study population, newborns with intrauterine infection, congenital malformations, genetic metabolic diseases, malignant tumors, or serious primary diseases affecting major organs, such as the heart, brain, and kidney, were excluded. Additionally, women with maternal autoimmune diseases or associated conditions that could impact the neonatal immune system were also excluded. All newborns diagnosed with acute FD met the clinical diagnostic criteria. Ethical approval for the study was obtained from the Clinical Ethics Review Committee of the Guangdong Provincial People's Hospital and the Nanfang Hospital of Southern Medical University.

Reagents and antibodies

The details of the reagents and antibodies used in this study are listed in Table S1 and Table S2.

Mice

All C57BL/6 and BALB/c mice were purchased from the Laboratory Animal Center of Southern Medical University. HIF-1α$^{fl/fl}$ mice were kindly provided by Prof. Zhe-Xiong Lian from Guangdong Academy of Medical Sciences (Guangzhou, China). S100A8^{cre} mice (Stock No: C001280) were purchased from Cyagen Biosciences Inc. (Suzhou, Jiangsu, China). HIF-1α$^{fl/fl}$ S100A8^{cre} mice were produced by breeding HIF-1α$^{fl/fl}$ mice with S100A8^{cre} mice and conducting genotyping PCR to detect the HIF-1α-flox and S100A8-Cre genes on postnatal day 6. Subsequently, sex-unspecified newborns from each litter were randomly selected for placement into control or hypoxia treatment groups on postnatal day 7 (P7). All mice were kept in a pathogen-free facility at the Southern Medical University under consistent environmental conditions, including a humidity level of (50 ± 5) %, a temperature of (24 ± 1) °C, a 12 h light-dark cycle, and unrestricted access to food and water.

Cell isolation

Isolation of human PBMCs and whole blood cells

For PBMC isolation, the whole peripheral blood was centrifuged, and the plasma was removed. The remaining blood cells were diluted using phosphate-buffered saline (PBS). In a 15 mL sterile centrifuge tube, 2 mL of lymphocyte separation solution was added. Next, 4 mL of the diluted peripheral blood was layered gently on top of the separation solution. The tube was then subjected to density gradient centrifugation at 25 °C and 400 ×g for 25 min. Following centrifugation, the white membrane layer containing PBMCs was transferred carefully to a new sterile centrifuge tube. To remove red blood cells (RBCs), an ammonium chloride-potassium (ACK) solution was used. The PBMCs were treated with ACK to lyse the RBCs. Subsequently, the PBMCs were collected and prepared for further experiments. For whole blood cell samples, the direct treatment involved the use of RBC lysis buffer (TONBO, China) to remove the RBCs. Cell suspensions were obtained after the lysis process and were used for the detection of the LOX1^{+} phenotype and subsequent experiments.

Isolation of mouse brain mononuclear cells

The experimental protocol was performed as described previously. Briefly, mouse brain tissue was removed, cut into small pieces, and digested in RPMI 1640 (BI, Israel) containing 1 mg/mL collagenase type IV (Gibco, USA) at 37 °C for 40 min. The brain pieces were filtered through a 70 cm cell strainer. Subsequently, cells were resuspended in 4 mL of 30% Percoll (GE, Sweden) and the resuspended cells were placed gently on top of a 2 mL 70% Percoll solution in a sterile centrifuge tube. The white membrane layer was aspirated after density gradient centrifugation at 25 ℃ and 400 ×g for 25 min. Cell suspensions were collected and prepared for subsequent analysis experiments.

Flow cytometric analysis

For extracellular staining, the single-cell suspension was stained with surface markers directly at 4 °C for 30 min. For intracellular staining, the cells were fixed and permeabilized with fixation and permeabilization buffers (BD Biosciences) for 30 min at 25 °C after surface staining. Next, cells were stained with transcription factors or target protein, followed by incubation with secondary antibody for 30 min at room temperature. A LSR Fortessa flow cytometer (BD Biosciences) was used for flow cytometry data acquisition, and the data were analyzed using FlowJo v10.0.7 (https://www.flowjo.com/solutions/flowjo/downloads). The flow cytometry in our work was supported by the Department of Immunology at the School of Basic Medical Sciences, Southern Medical University. In humans, the gating strategy of PMN-MDSCs

is defined as $CD45^+$ $CD11b^+$ $CD15^+$ $CD14^-$, and the gating strategy of M-MDSCs is defined as HLA-$DR^{low/-}$ $CD45^+$ $CD11b^+$ $CD15^-$ $CD14^+$. The strategy for human $LOX1^+$ PMN-MDSC gating from whole blood samples was $CD45^+LOX1^+$ $CD15^+$ [43]. In mice, the phenotype of PMN-MDSCs is defined as $CD45^+CD11b^+$ $Ly6G^+Ly6C^{Low/-}$, and the phenotype of M-MDSCs is defined as $CD45^+CD11b^+Ly6G^-Ly6C^{High}$.

Cell sorting

Single-cell suspensions were firstly cultured with specific biotin antibodies against human/mouse lineage markers as follows: CD3, CD4, CD8, CD19, CD11c, CD16, CD34, CD123, FceRa, TCRα/β and TCR- γ/δ for human; and CD3e, CD5, CD4, CD8, CD11c, CD19, F4/80, NK1.1, CD19, TER119, TCR β and TCR γ/δ for mice. The cell-antibody mixture was then incubated with streptavidin-paramagnetic particles (BD Biosciences) at 4 °C for 30 min. Subsequently, the obtained lineage-negative cells were labeled with anti-human LOX1-APC or anti-mouse Ly6G-APC antibodies, followed by further sorting using the EasySep Human/mouse APC-positive selection kit II (StemCell, Canada) to isolate $LOX1^+$PMN-MDSCs or $Ly6G^+$ PMN-MDSCs. For mouse $CD3^+$ T cell sorting, splenocyte suspensions were labeled with anti-mouse CD3 biotin antibodies (BioLegend). To sort the mouse microglia, brain cell suspensions were labeled with an anti-mouse CD11b antibody [44]. The cell-antibody mixture was then incubated with streptavidin-paramagnetic particles (BD Biosciences) at 4 °C for 30 min. All acquired cells were sorted to 95% purity.

Wright-Giemsa staining

To compare the morphological characteristics of $LOX1^+$ PMN-MDSCs, $LOX1^+$ PMN-MDSCs were isolated from the whole blood of NNB and FDNB and stained with Wright-Giemsa staining solution (GBCBIO, China) according to the manufacturer's protocol.

Immunosuppressive function assay of neonatal PMN-MDSCs

T-cell proliferation assay with depletion of $LOX1^+$ PMN-MDSCs

After removal of red blood cells, the total cells (TC, including $LOX1^+$ PMN-MDSCs) from newborns were stained with CFSE (Thermo Fisher, USA) at 37 °C for 15 min. After the depletion of $LOX1^+$ cells, the remaining cells were defined as Total cells excluding $LOX1^+$ PMN-MDSCs. The cells were then stimulated with anti-CD3/CD28 functional antibodies for 72 h. The unstimulated $TC^{depletion}$ group served as a negative control. After incubation for 72 h, the supernatants were collected to measure the secretion of IFN-γ.

Concentration-dependent T-cell proliferation assay in mice

$CD3^+$ T cells were isolated from the spleens of BALB/c mice and then labeled with CFSE for 15 min at 37 °C. $Ly6G^+$ cells were isolated from the spleens of both CNB and HNB. These cells were cocultured in 96-well plates at different ratios in RPMI 1640 (10% FBS) and stimulated with Concanavalin A (Con A, 5 μg/mL); unstimulated T cells were used as a negative control. Before flow cytometry, the cells were collected and stained with anti-CD4 and anti-CD8a antibodies, and T cell proliferation was assessed based on the intensity of CFSE fluorescence [45].

Hypoxic-ischemic encephalopathy (HIE) models

Hypoxic-ischemic encephalopathy (HIE) models typically incorporate both hypoxia and carotid artery ligation (CCA) [46–48]. In brief, postnatal day 7 (P7) mice were anesthetized with isoflurane. The right common carotid artery was exposed and ligated using double-layered 7 – 0 sutures. After the procedure, the mice were returned to their mothers for two hours. They were then placed in a hypoxic chamber with 8% O_2 and 92% N_2 at 37 °C for an additional two hours to induce hypoxia following ischemia. After this exposure, the neonatal mice returned to their mothers and assessed post-survival rates.

Hypoxia-induced mouse models

The detailed animal model of acute hypoxia has been described previously [49, 50]. In brief, 7-day-old neonate mice were exposed randomly to hypoxia at 0% O_2, 100% N_2 in a hypoxic chamber for 7 min. Next, they were placed in a 21% O_2, 78% N_2 environment for reoxygenation and returned to their dams. To obtain target cells, the pups were sacrificed at different time points (12, 24, 48, and 72 h) after hypoxia. The hypoxia model of newborn mice (HNB) served as the experimental group, and control newborn mice (CNB) served as the control group. Peripheral blood, spleen, and brain samples were collected from both groups for further analysis. Additionally, gene knockout newborn mice (HIF-$1\alpha^{fl/fl}$ $S100A8^{cre}$ mice) were subjected to hypoxia using the same procedure described above. The mice were euthanized at 48 h following hypoxia induction to obtain cells from the blood, spleen, and brain for subsequent analysis.

PMN-MDSCs depletion experiment

To deplete PMN-MDSCs, 40 mg/kg of anti-Ly6G (Ly6G mAb, BioXcell, USA) was given to 6-day-old neonate mice by intraperitoneal injection. Rat IgG2b isotype (IgG2b mAb, BioXcell, USA) was used as the control. The mice were subjected to hypoxia induction after 24 h. Subsequently, mice were sacrificed at 48 h after hypoxia induction to assess various indicators, including the phenotype of PMN-MDSCs in peripheral blood and spleen,

the phenotype of microglial cells, and their subsets in the brain, and histopathological examination of brain tissue was performed.

Adoptive transfer of PMN-MDSCs

For PMN-MDSCs transfer in the acute hypoxia model, a total of 5×10^5 splenic PMN-MDSCs from neonatal hypoxia treated HIF-1$\alpha^{fl/fl}$ mice or HIF-1$\alpha^{fl/fl}$ S100A8^{cre} mice were administered intraperitoneally to recipient mice (7-day neonatal WT mice) 1 h before hypoxia induction. The mice were sacrificed 24 h after hypoxia induction to assess various indicators, including the phenotype of microglia and its subsets in the brain, and histopathological examination of brain tissue was carried out.

Administration of lactate

Seven-day-old pups were assigned randomly to each of the two experimental groups: HIF-1$\alpha^{fl/fl}$ S100A8^{cre} mice group, HIF-1$\alpha^{fl/fl}$ S100A8^{cre} mice + Lactate group. Lactate was dissolved in phosphate-buffered saline (PBS) at pH 7.4. Lactate or vehicle was injected intraperitoneally at a dose of 2 g/kg body weight before hypoxia induction for 1 h (Once a day for two consecutive days). The mice were sacrificed 48 h after hypoxia induction to assess various indicators, including the phenotype of microglia and their subsets in the brain, and a histopathological examination of the brain tissue was conducted.

TTC (2,3,5-Triphenyltertrazolium chloride) staining

In the hypoxia model, the infarct volume was assessed by 2% TTC (Sigma-Aldrich, USA) staining [46]. Initially, mice were anesthetized with 2% isoflurane, decapitated, and their brains were promptly frozen at -30 °C for 10 min. Because of the fragile and small brains of 7-day-old mice, each brain was sliced into three 2-mm sections, which were incubated in TTC solution for 15 min protect from light, flipped every 5 min, and fixed in 4% paraformaldehyde (PFA) to assess the infarct volume. The infarct area comprised a pale gray region, representing infarcted tissue, and a dark red area, indicating normal brain tissue. A single representative dataset is presented. The total infarct volume was calculated by summing the infarct areas across the three brain slices. The calculation was performed in an unbiased and blinded manner. Infarct area analysis was performed using ImageJ software and the percentage of infarct area was determined using the following formula: (infarct area/total brain tissue area) × 100%.

Brain water content

The brain water content (BWC) was assessed as previously described [47]. Four mice were used in each group, and the BWC (%) was calculated using the formula: (wet weight - dry weight) / wet weight × 100%. The wet weight of the brain tissue was measured immediately after removal from the animal. Subsequently, it was placed in a constant-temperature oven at 60 °C for approximately 48 h to obtain the dry weight.

Assessment of short-term neurological function (geotaxis reflex time)

Assessment of short-term neurological function has been previously documented [48]. In brief, negative geotropism was evaluated 48 h post-hypoxia model by two blinded investigators in an unbiased setting, utilizing four mice per group. The assessment involved positioning the neonatal mice head-down on a tilt board inclined at a 45° angle, followed by recording the time taken for the animal to turn and achieve a head-up position. The duration of the test was limited to a maximum of 60 s.

Histopathological analysis

Brain tissues were fixed in 4% paraformaldehyde for more than 24 h. After dehydration, the samples were embedded in paraffin and sliced into 6 μm slices. Paraffin sections were stained with hematoxylin and eosin (H&E) stain (Solarbio, China) and Nissl (Sangon Biotech, China), according to the manufacturer's protocols. Hippocampal neuronal damage was assessed using a standard semi-quantitative scale with some modifications [51]. Briefly, 0 indicated no lesions in the hippocampal Cornu Ammonis (CA) region and dentate gyrus (DG) cell layers, 1 indicated scattered damaged neurons in the hippocampal CA region, 2 indicated a moderate number of damaged neurons in the hippocampal CA region (< 50% neurons affected), 3 indicated severe damage in the hippocampal CA region (> 50% of damaged cells), and grade 4 indicated extensive neuronal damage in the hippocampal regions. The evaluation was performed by an investigator who was blinded to each group. The number of positive cells in the hippocampus was observed and recorded using the NIS viewer (NIS-Elements Viewer 4.50, Tokyo, Japan) under an optical microscope (NIKON) at 400× magnification.

Immunofluorescent staining

The procedures were adapted from those previously described [52]. Mice were anesthetized using 1% pentobarbital sodium, after which their brains were extracted and post-fixed in 4% paraformaldehyde for a duration of 12 h. Subsequently, the tissues were equilibrated in a solution of 30% sucrose. Coronal sections with a thickness of 10 μm, encompassing the hippocampus, were then collected. Brain slices were incubated in a blocking solution containing 5% bovine serum albumin and 1% Triton X-100 for one hour at room temperature, followed by an overnight incubation at 4 °C with primary antibodies: rabbit anti-NeuN (1:500, Cell Signaling Technology,

Cat#12943) or rabbit anti-IBA1 (019-19741, Wako, 1:500). The following day, the slices were incubated for two hours at room temperature with secondary antibodies including PE-conjugated goat anti-rabbit (Invitrogen), TUNEL staining reagent (Beyotime), or PE-anti-mouse CD68 (137013, BioLegend; dilution of 1:50). After three washes with PBS, the samples were treated with DAPI (Invitrogen) for ten minutes and subsequently washed three more times. Finally, the slices were mounted onto microscope slides. Fluorescent images were captured using a confocal microscope (A1R; Nikon). Cell counting and fluorescent area measurements were performed utilizing ImageJ software.

Behavioral analysis

Behavioral tests were conducted to assess motor function of seven-day-old HIF-1$\alpha^{fl/fl}$ S100A8^{cre} mice as described [53]. The definitions of the test and the associated scoring system are outlined as follows: (1) Walking ability test: A score of 0–3 is used to evaluate the walking ability of a pup. (no movement = 0; asymmetrical crawling = 1; slow crawling but symmetrical limb movements = 2; fast crawl/walk = 3); (2) Hindlimb suspension test: a pup is placed in a cage with its hind legs slightly suspended over the edge of the cage to assess its hind limb strength. A score of 0–4 was used to evaluate hind limb strength (normal separation of the hind limbs with a raised tail = 4; weakness with closer hind limbs = 3; weakness with hind limbs frequently touching each other = 2; hind limbs almost always clenched with the tail raised = 1; hind limbs always clenched with the low tail or unable to grasp the cage edge = 0); (3) Surface righting test: the time taken for a pup to return from supine to prone; and (4) Negative geotaxis test: the time taken for a pup to turn its face up on a downward slope.

Enzyme-linked immunosorbent assay

Arginase activity was calculated according to the manufacturer's instructions and previous studies [45]. Briefly, the cells were lysed with radio immunoprecipitation assay (RIPA) lysis buffer (pH 7.4) (Beyotime, China). After adding L-arginine and $MnCl_2$, the cell lysate was incubated at 37 ℃ for 2 h, and urea concentration was measured at 450 nm according to the manufacturer's instructions. In addition, cell lysates were collected to evaluate PGE2 concentration (catalog no. E-EL-0034c, Elabscience) and lactate concentrations were analyzed after deproteinization using lactate colorimetric/fluorometric assay kits (Elabscience, China). Furthermore, an ELISA KIT (4 A Biotech, China) was used to detect the levels of some cytokines (IL-10, TGF-β, IL-1β, IFN-γ) in the plasma of human newborns. The sample absorbances were measured using a plate reader and quantified from a generated standard curve (in pg/mL) following manufacturers' instructions.

Seahorse metabolic flux analysis

The extracellular acidification rate (ECAR) and oxygen consumption rate (OCR) were measured using a Seahorse XFe96 Analyzer (Agilent Technologies). Briefly, 1×10^5 blood LOX-1$^+$PMN-MDSCs sorted from newborn blood, or 1×10^5 splenic PMN-MDSCs sorted from hypoxia-treated mice at different time points, or 3×10^4 splenic PMN-MDSCs sorted from hypoxia-treated knockout mice were transferred into Cell-Tak (Corning)-coated XF96 cell culture microplates. The medium was supplemented with 1 mM sodium pyruvate, 2 mM glutamine, and 10 mM d-glucose and incubated at 37 °C for 1 h in a non-CO_2 incubator, with the pH adjusted manually to 7.4. Three consecutive ECAR (mpH/min) measurements were obtained in XF-supplemented media at 37 °C under basal conditions in response to 2 μM oligomycin, 50 mM glucose, and 20 mM 2-DG, 1.5 μM carbonyl cyanide- 4- (trifluoromethoxy) phenylhydrazone (FCCP), 1 μM rotenone, and 1 μM antimycin A (R/A). Glycolysis and glycolytic capacity were calculated as the average of three measurements after adding glucose and oligomycin, respectively. Basal and maximal OCR were calculated from the average of three measurements before the addition of oligomycin and after the addition of FCCP, respectively. SRC was calculated as the difference between basal and maximal OCR. Data were analyzed using Wave software (Agilent v.2.6.1) [54].

Cell lines and co-culture experiment

Human microglia cell lines (HMC3) and mouse microglia cell lines (BV2) were cultured in Dulbecco's modified eagle medium (DMEM) media (BI, Israel) supplemented with 10% fetal bovine serum (FBS) and 1% penicillin/streptomycin (BI, Israel) at 37 °C and 5% CO_2 in an incubator. The cells were digested with trypsin-EDTA Solution A (BI, Israel) for 2 min, and when the density reached up to 90%, the cells were collected for subculture or further analysis. To evaluate the impact of lactate derived from PMN-MDSCs on the expression of inflammatory factors in microglia, we cocultured microglia isolated from brain tissue or microglial cell lines with different concentration of lactate (5 mM and 10 mM). After a 72-hour incubation, the expression levels of inflammatory factors within the microglia were assessed using flow cytometry.

RT-qPCR

For real-time quantitative reverse transcription PCR (RT-qPCR), total RNA was extracted using TRIzol (Invitrogen, USA), and reverse transcription was performed using a StarScript II One-Step RT-PCR Kit (Genstar,

China). The target genes were measured using a QuantStudio 6 Flex system (Thermo Fisher Scientific, USA) and a RealStar Green Power Mixture kit (Genstar, China). The expression level of mRNA was normalized by β-actin, and the minimum expression level of the control group was artificially set at 1. The relative mRNA expression of other genes was measured using the standard $2^{-\Delta\Delta CT}$ method. The PCR primer sequences used in this study are listed in Table S3.

Chromatin Immunoprecipitation (ChIP) assay

A total of 2.0×10^6 PMN-MDSC cells were sorted from newborn blood, hypoxia-treated mice at different time points, or knockout mice. 10% of the lysate before immunoprecipitation was used as an input control and ChIP was conducted as previously described [55]. Briefly, PMN-MDSCs were fixed with a 1% formaldehyde solution, cross-linked with 0.125 mol/L glycine, lysed using ultrasound, and then sheared by sonication. Agarose gel electrophoresis (1.5%) was used to gauge the size of the chromatin fragments after sonication. Cell lysates were pre-cleared with protein antibody-chromatin complexes and collected by incubation with protein A/G-agarose beads. The supernatant was collected and DNA was purified by phenol-chloroform extraction and ethanol precipitation. After DNA purification, qPCR was performed using the primers listed in Table S3. The data were normalized against the input DNA and presented as an enrichment fold-increase over the IgG control.

Western blotting

Cells were harvested and subjected to western bolt analysis, as described previously [56]. Firstly, PMN-MDSC cells sorted from newborn blood, or hypoxia-treated mice at different time points, or knockout mice were lysed with RIPA lysis buffer (Beyotime, China). The protein concentration was measured using the Bicinchoninic Acid Protein Assay Kit (Beyotime, China). Subsequently, 30 micrograms protein/lane was separated by sodium dodecyl sulfate polyacrylamide gel electrophoresis (SDS-PAGE), and the target protein was transferred onto polyvinylidene difluoride (PVDF) membranes (Millipore, USA). After 1 h of blocking with milk, the membrane was incubated with the corresponding primary antibody at 4 ℃ overnight followed by incubation with HRP-conjugated secondary antibody at room temperature for 1 h. Next, protein bands were labeled with chemiluminescent solution (Millipore, USA), and chemiluminescence signals were detected using ChemiDoc™ XRS+ (BioRad, USA).

RNA-sequencing data analysis

For RNA-seq analysis, PMN-MDSC cells sorted from different newborn blood groups (NNB group and FDNB group) were used for transcriptome analysis. RNA-seq library construction and sequence analysis services were performed by the BGI-Wuhan Corporation (Shenzhen, China). Each microarray sample correlation value was normalized to the Pearson correlation versus the average RNA-seq profile. Relative mRNA expression levels were calculated based on the exon regions using Cufflinks and the mm10 reference genome annotations. Differentially expressed genes (DEGs) identified using DESeq2 (fold change > 1.5, $P < 0.05$) were highlighted in the Gene Set Enrichment Analysis (GSEA) plot and used for the Kyoto Encyclopedia of Genes and Genomes (KEGG) analysis, and Gene Ontology (GO) analysis. All heat maps were generated using an integrative toolkit software.

Statistical analyses

All experimental data were analyzed using GraphPad Prism 8.0 software (GraphPad Software Inc., San Diego, CA, USA). After comparing the distribution of variables, two-tailed unpaired Student's *t*-tests or nonparametric Mann–Whitney U tests were used for statistical comparison between the two groups. For multigroup comparisons, One-way Analysis of Variance with Tukey's test was employed. Correlation analysis was conducted to identify the association between two sets of variables for human experiments. Spearman's correlation coefficient, with significance (p), are reported for each correlation, and regression lines are depicted. "*" indicates *P*-values and "ns" indicates no significance. Differences were considered statistically significant when the *P*-values were < 0.05. $^*P < 0.05$; $^{**}P < 0.01$; $^{***}P < 0.001$; $^{****}P < 0.0005$.

Results

Enhanced activation of FDNB peripheral blood LOX1+ PMN-MDSCs with increased anti-inflammatory signals in circulation

Several studies have highlighted the elevated levels of MDSCs in neonates, which play a role in reducing intestinal inflammation by balancing pro-inflammatory and anti-inflammatory responses [24, 25, 57]. The risks of FDNB have been reported widely [58]; however, the role of MDSCs in FDNB remains unclear. Using traditional definitions of human MDSC subsets [24], we first assessed the proportion and absolute number of MDSCs in peripheral blood mononuclear cells (PBMCs) isolated from newborns with normal delivery (NNB) and newborns with fetal distress during delivery (FDNB). The proportion and absolute number of $CD11b^+CD15^+CD14^-$ cells (PMN-MDSCs) in the FDNB group were significantly higher than those in the NNB group (Fig. S1A, B); however, no significant difference was observed in $CD11b^+HLA\text{-}DR^{low/-}CD15^-CD14^+$ cells (M-MDSCs) (Fig. S1C, D). Additionally, we analyzed other immune cells in peripheral blood. The results showed a significant

decrease in the proportion of $CD4^+$ T cells in the FDNB group compared to the NNB group (Fig. S1E). The proportions of other common immune cells (including $CD8^+$ T cells, B cells, NK cells, monocytes, DCs, Th1 cells, Th17 cells, and Tregs) were not significantly different between the NNB and FDNB groups (Fig. S1F-M).

Previous reports have shown significant activation of $LOX1^+$ PMN-MDSCs in newborn whole blood [24]. Therefore, we examined the levels of $LOX1^+$ PMN-MDSCs in both groups. The results showed a significant increase in the proportion and absolute number of $LOX1^+$ PMN-MDSCs ($LOX1^+CD15^+$ cells) in the whole blood of the FDNB group compared to that in the NNB group (Fig. 1A, B). In addition, $LOX1^+$ PMN-MDSCs in the FDNB group exhibited band-shaped nuclei, consistent with the specific morphological characteristics of PMN-MDSCs observed in previous studies (Fig. 1C). To explore the immunosuppressive function of $LOX1^+$ PMN-MDSCs in FDNB, we performed a depletion assay of $LOX1^+$PMN-MDSCs. The results demonstrated significant decrease in the proliferation rates of $CD4^+$ T cells and $CD8^+$ T cells, as well as reduced IFN-γ production in FDNB compared to NNB, indicating enhanced immunosuppressive function of $LOX1^+$ PMN-MDSCs in FDNB (Fig. 1D, E; S2A). Subsequently, MDSC-targeting genes were verified by sorting $LOX1^+$ PMN-MDSCs from NNB and FDNB blood samples. The mRNA levels of *S100A8*, *S100A9*, *ARG1*, and *COX2* in $LOX1^+$ PMN-MDSCs from FDNB were significantly higher than those from NNB (Fig. 1F), whereas no change was observed in *iNOS* and *CYBB* (Fig. S3A). Western blotting showed that the expression of S100A9, ARG1, and COX2 in $LOX1^+$ PMN-MDSCs from FDNB was significantly higher than that from NNB (Fig. 1G). Similarly, the mean fluorescence intensity (MFI) of S100A9, arginase activity, and PGE2 production in $LOX1^+$ PMN-MDSCs from FDNB were significantly higher than those from NNB (Fig. 1H-J). However, ROS levels remained unchanged between the two groups (Fig. S3B). These findings demonstrate the expansion and activation of $LOX1^+$ PMN-MDSCs in the peripheral circulation of FDNB.

Considering the distinct responses of female and male neonatal brains to hypoxic injury, a comparison was made regarding the proportion of PMN-MDSCs in FDNB blood samples from both sexes was compared. After further statistical analysis of PMN-MDSC phenotypes, no differences were observed (Fig. S4A). Subsequently, analysis of clinical data obtained from 103 neonates with FDNB using comprehensive brain magnetic resonance imaging (MRI) reports showed that among the FDNB group, 79 cases exhibited no significant abnormalities in the cranial cavity, correlating with a high proportion of PMN-MDSCs. However, in 24 cases in which brain MRI results indicated features such as microbleeding lesions or subdural hemorrhage, lower levels of PMN-MDSCs were observed (Fig. S4B, C). These observations suggest a clear correlation between brain injury and the ratio of PMN-MDSCs, prompting further exploration of their roles. Subsequently, further analysis of neonatal clinical cases from the FDNB revealed that neonates with brain injury had significantly higher NSE levels than neonates without brain injury (Fig. 1K). Correlation analysis demonstrated a significant negative correlation between the frequency of $LOX1^+$ PMN-MDSCs and NSE levels (Fig. 1L). Moreover, the frequency of $LOX1^+$ PMN-MDSCs was significantly and positively correlated with the Test of Infant Motor Performance (TIMP) score, which serves as an early screening index for neonatal brain injury (Fig. 1M). These results further indicate that PMN-MDSCs play a key role in the resistance to neonatal brain injury. The frequency of $LOX1^+$ PMN-MDSCs was also significantly negatively correlated with C-reactive protein (CRP) (Fig. 1N), length of hospital stays in neonates (Fig. 1O), and procalcitonin (PCT) (Fig. 1P). Notably, we also observed that the ratio of $LOX1^+$ PMN-MDSCs was significantly positively correlated with "neutrophil counts" (Fig. 1Q). More interestingly, the contents of IL-10 and TGF-β in plasma from FDNB were significantly increased and the levels of IL-1β and IFN-γ in plasma from FDNB were significantly decreased when compared with those from NNB (Fig. 1R). These findings indicate that the enhanced activation of $LOX1^+$ PMN MDSC in the peripheral blood of newborns with FDNB occurred concurrently with further enhancement of anti-inflammatory signals in the peripheral circulation.

HIF-1α accumulation in $LOX1^+$ PMN-MDSCs from FDNB enhances glycolysis and lactate production

To identify the regulatory mechanisms of FDNB, $LOX1^+$ PMN-MDSCs from NNB and FDNB were collected for RNA sequencing. The analysis revealed 3376 differential gene expressions (FDR < 5%) in $LOX1^+$ PMN-MDSCs between the NNB and FDNB groups (Fig. S5A). Among them, 1537 genes were upregulated, and 1839 genes were downregulated in $LOX1^+$ PMN-MDSCs from FDNB compared to those from NNB (Fig. S5B, C). First, PMN-MDSC-related target genes (*S100A8*, *S100A9*, *ARG1*) were upregulated (Fig. 2A, S5D), which is consistent with the mRNA results. In addition, expression of genes involved in glycolysis (*PFKFB2*, *PFKFB3*, *PFKFB4*, *GPI*, *ALDOA*, *ALDOC*, *PKM*, *LDHA*) and the lactate transporter (*SLC16A3*) was upregulated in FDNB (Fig. 2A). KEGG analysis showed that the upregulated genes were enriched in HIF-1 signaling pathways (Fig. 2B). Additionally, GO analysis classified the differentially expressed genes based on biological processes and revealed that the up-regulated genes belonged predominantly to the hypoxia-inducible factor-1 alpha (HIF-1α) signaling

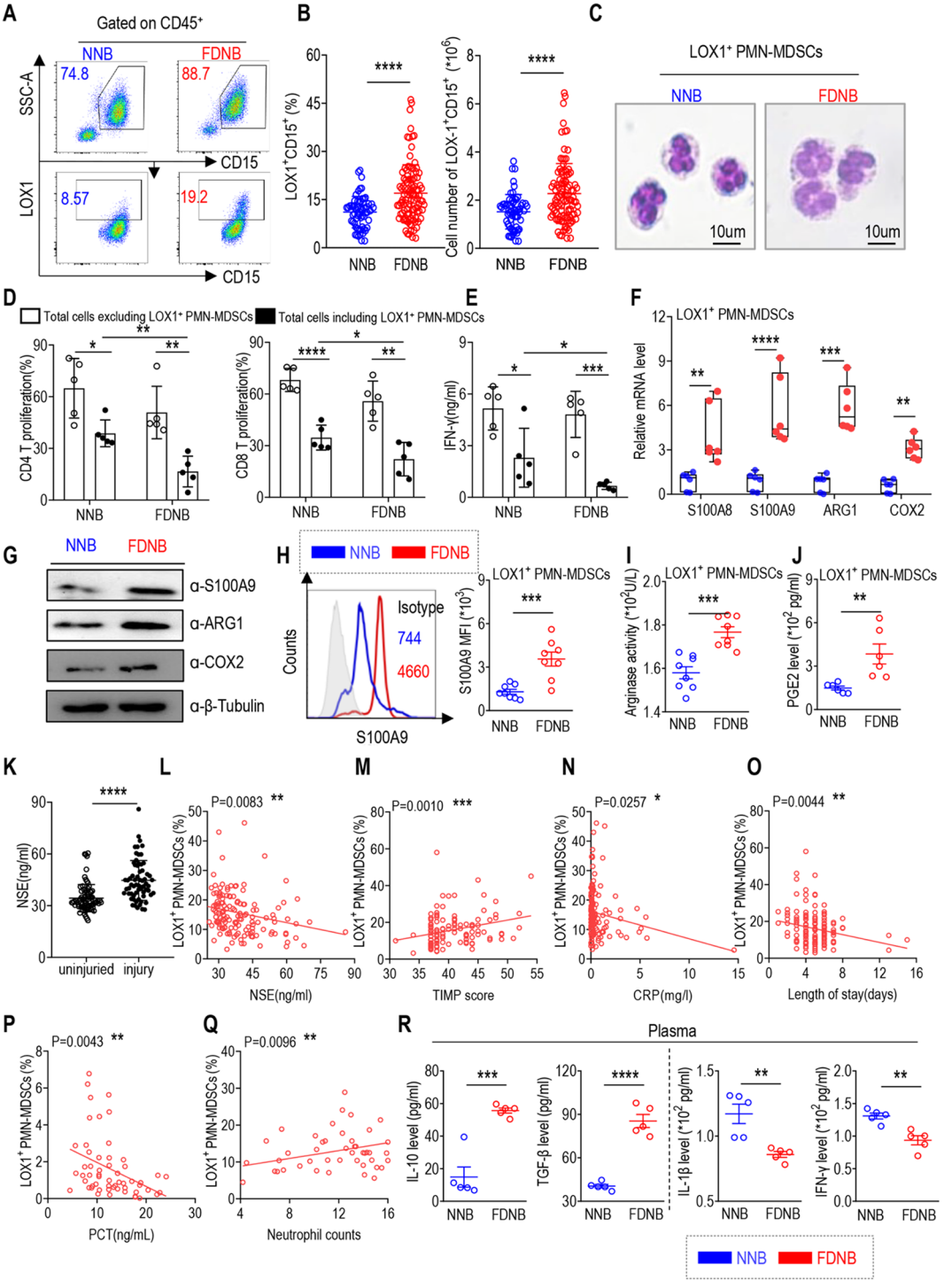

Fig. 1 (See legend on next page.)

(See figure on previous page.)

Fig. 1 Enhanced activation of FDNB peripheral blood LOX1 + PMN-MDSCs with increased anti-inflammatory signals in circulation. (**A**) Representative flow cytometry results and (**B**) statistical analysis of the proportion (left) and absolute number (right) of $LOX1^+$ PMN-MDSCs in the whole blood from newborns with normal delivery (NNB, $n = 61$; female, $n = 34$; and male, $n = 27$) and newborns with fetal distress during delivery (FDNB, $n = 103$; female, $n = 54$; and male, $n = 49$). (**C**) Typical morphology of $LOX1^+$ cells from NNB and FDNB. (**D**) Statistical analysis of the proliferation rates of $CD4^+$ T cells and $CD8^+$ T cells from NNB and FDNB. Total cells including PMN-MDSCs and total cells excluding PMN-MDSCs were stimulated with anti-CD3/CD28 functional antibodies for 72 h, and the proliferation of T cells was examined by CFSE staining ($n = 5$). (**E**) IFN-γ secretion level of TC and $TC/LOX1^{depletion}$ from NNB and FDNB ($n = 5$). $LOX\text{-}1^+$ PMN-MDSCs sorted from NNB and FDNB blood (**F-J**): (**F**) mRNA levels of *S100A8*, *S100A9*, *ARG1*, and *COX2* ($n = 6$). (**G**) Protein levels of *S100A9*, *ARG1*, and *COX2* were measured by western blotting experiment. (**H**) Representative flow cytometry results (left) and statistical analysis (right) of S100A9 level ($n = 8$). (**I**) Level of arginase activity ($n = 8$). (**J**) PGE2 Level ($n = 6$). (**K**) NSE levels of plasma in neonates with and without brain injury (uninjured, $n = 80$; injury, $n = 65$). (**L-Q**) Correlation analysis of $LOX1^+$ PMN- MDSCs and plasma NSE level in FDNB ($n = 146$). (**M**) Correlation analysis of $LOX1^+$ PMN-MDSCs and TIMP scores in FDNB ($n = 135$). (**N**) Correlation analysis of $LOX1^+$ PMN-MDSCs and plasma CRP level in FDNB ($n = 151$). (**O**) Correlation analysis of $LOX1^+$ PMN-MDSCs and the length of stay in FDNB ($n = 155$). (**P**) Correlation analysis of $LOX1^+$ PMN-MDSCs and plasma PCT level in FDNB ($n = 56$). (**Q**) Correlation analysis of $LOX1^+$ PMN-MDSCs and the neutrophil counts in FDNB ($n = 59$). (**R**) Expression level of IL-10, TGF-β, IL-1β, and IFN-γ in plasma from NNB and FDNB groups ($n = 5$). Data are pooled from two independent experiments; $^*P < 0.05$; $^{**}P < 0.01$; $^{***}P < 0.001$; $^{****}P < 0.0001$. Bar graphs show the mean ± SEM. Statistical significance was determined using a two-tailed unpaired Student's *t*-test (**B, D–F, H-K**, and **R**). Spearman's correlation coefficient and significance (p) are noted for each correlation in (**L-Q**), and regression lines are shown

pathway (Fig. 2C). These results strongly suggest a close association between $LOX1^+$ PMN-MDSCs and glycolysis, with the involvement of HIF-1 signaling in the activation of $LOX1^+$ PMN-MDSCs in FDNB.

To validate the RNA sequencing findings, we isolated $LOX1^+$ PMN-MDSCs from NNB and FDNB groups and assessed HIF family gene mRNA expression. Our analysis showed no significant differences between the two groups (Fig. S6A). Protein expression analysis revealed no changes in HIF-2α or HIF-1β levels; however, we observed a notable increase in HIF-1α protein levels in $LOX1^+$ PMN-MDSCs from the FDNB group compared to those from the NNB group (Fig. 2D-F, S6A). This finding aligns with published literature indicating that exposure to hypoxic conditions results in a substantial increase in HIF-1α protein level, despite unchanged mRNA level. This phenomenon can be attributed to that, under normal condition, the von Hippel-Lindau tumor suppressor protein (VHL) binds to HIF-1α, promoting its ubiquitination and subsequent rapid degradation. While the application of MG132 in vitro inhibits the degradation of HIF-1α [59, 60]. To address this issue, HIF-1α stabilization experiments were performed. Data showed that the addition of MG132 significantly enhanced the expression levels of HIF-1α protein in PMN-MDSCs from the NNB (Fig. S6B). This finding corroborates the elevated expression of HIF-1α protein following hypoxic conditions. Additionally, the mRNA levels of glycolysis-related genes such as *PFKFB2*, *PFKFB3*, *PFKFB4*, *GPI*, *ALDOA*, *ALDOC*, *PKM2*, and *LDHA* in $LOX1^+$ PMN-MDSCs from FDNB were significantly higher than those from NNB, which was consistent with the gene set enrichment analysis (GSEA) results (Fig. 2G, H). We also observed enhanced expression of lactate transport-related genes, such as *SLC16A3*, rather than *GPR81* or *SLC16A1* in FDNB (Fig. 2G, S6C). Subsequently, the bioenergetic profile of activated PMN-MDSCs was characterized by assessing the extracellular acidification rate (ECAR) and cellular oxygen consumption rate (OCR), which serve as indicators of mitochondrial respiration and glycolysis. Notably, seahorse assays demonstrated that PMN-MDSCs from the FDNB group exhibited significantly enhanced glycolytic capacity compared to those from the NNB group (Fig. 2I-K). However, changes in oxidative phosphorylation (OXPHOS) appeared to be relatively modest compared to the alterations observed in glycolysis (Figs. S7A-B). Consequently, our focus shifted towards glycolysis, and we did not concentrate on OXPHOS changes in subsequent experiments. Importantly, increased lactate secretion by PMN-MDSCs was observed in the FDNB group (Fig. 2L). In summary, we noted an accumulation of HIF-1α protein, which was accompanied by an enhancement in glycolytic metabolic activity within the FDNB context.

Furthermore, we investigated whether the genes S100A8, S100A9, ARG1, LDHA, and SLC16A3 could be identified as direct targets of HIF-1α within PMN-MDSCs. Initially, we searched the JASPAR database and confirmed potential binding sites between HIF-1α and function-related genes in PMN-MDSCs (including S100A8, S100A9, and ARG1), as well as genes involved in lactate production and transport (including LDHA and SLC16A3) (Fig. S8A). Subsequently, ChIP assays validated the binding of HIF-1α to these loci in PMN-MDSCs (Fig. S8B). Interestingly, an enhanced binding capacity to genes, including S100A8, S100A9, ARG1, LDHA, and SLC16A3, was observed in FDNB-derived PMN-MDSCs compared to the NNB group (Fig. 2M). Consequently, both function-related genes of PMN-MDSCs and lactate transport genes were identified as downstream transcriptional targets of HIF-1α in neonatal PMN-MDSCs.

Enhanced activation of splenic PMN-MDSCs alleviates brain injury and reduces microglial activation and inflammatory factor expression

Hypoxic-ischemic encephalopathy (HIE) models typically incorporate both hypoxia and carotid artery ligation

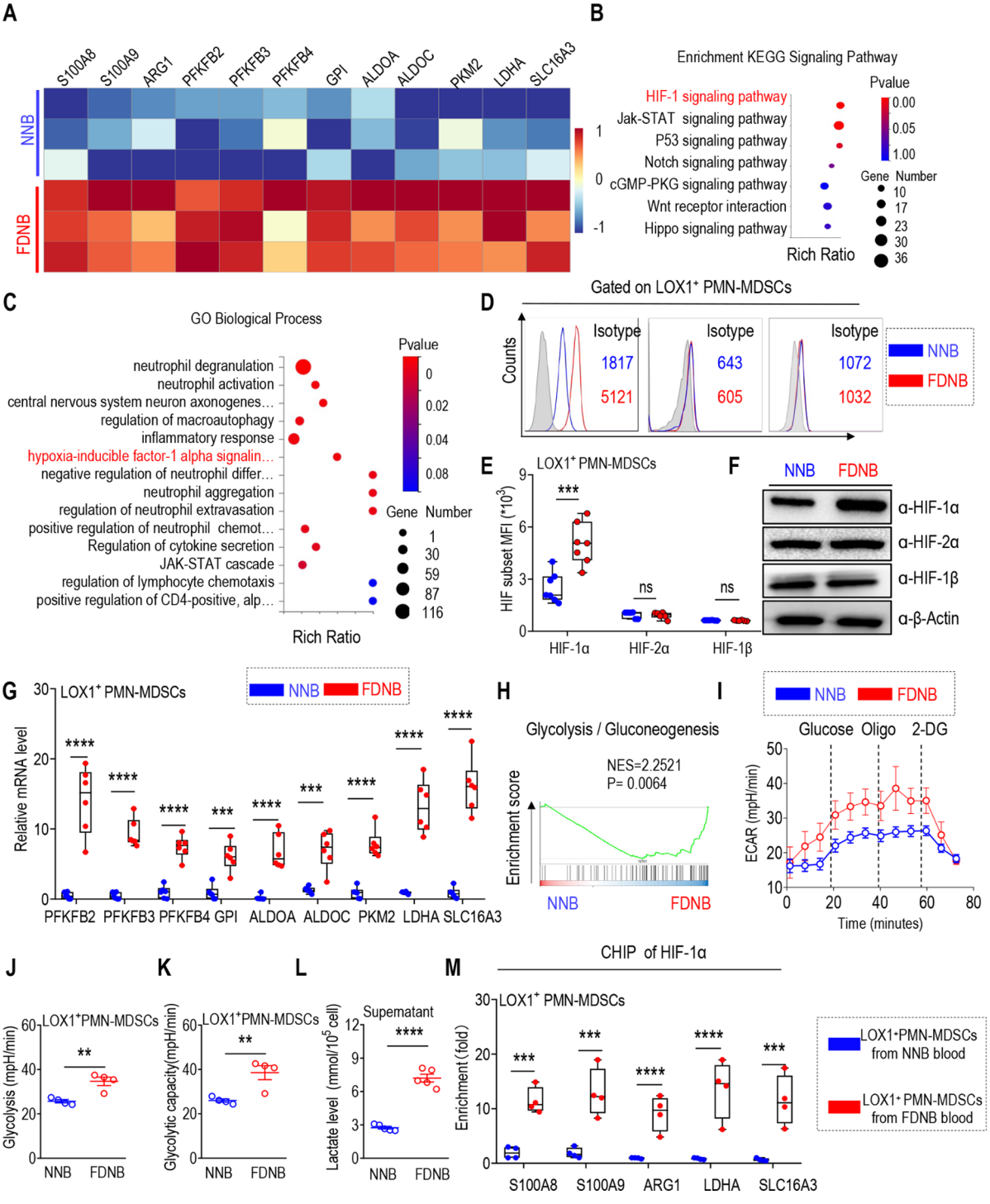

Fig. 2 (See legend on next page.)

(See figure on previous page.)

Fig. 2 HIF-1α accumulation in LOX1$^+$ PMN-MDSCs from FDNB enhances glycolysis and lactate production. (**A**) Heatmap showing the expression profile of LOX1$^+$ PMN-MDSCs from NNB and FDNB in up-regulated genes. (**B**) KEGG pathway analysis for the up-regulated genes in LOX1$^+$ PMN-MDSCs between NNB and FDNB groups. (**C**) GO analysis of biological process for the up-regulated genes in LOX1$^+$ PMN-MDSCs between NNB and FDNB groups. (**E**) Representative flow cytometry results (upper) and statistical analysis (lower) of HIF-1α ($n=7$), HIF-2α ($n=6$), and HIF-1β ($n=6$) level in PMN-MDSCs from NNB and FDNB blood. (**E, F**) Protein levels of HIF-1α, HIF-2α, and HIF-1β in LOX1$^+$ PMN-MDSCs from NNB and FDNB were tested by western blotting experiment. (**G**) mRNA levels of genes involved in glycolysis metabolism (*PFKFB2*, *PFKFB3*, *PFKFB4*, *GPI*, *ALDOA*, *ALDOC*, *PKM*, *LDHA*) and lactate transport (*SLC16A3*) in LOX1$^+$ PMN-MDSCs from NNB and FDNB ($n=6$). (**H**) Gene Set Enrichment Analysis (GSEA) plots show that glycolysis was upregulated in FDNB. (**I–K**) Seahorse analysis of extracellular acidification rate (ECAR) of glycolysis (**J**) and glycolysis capacity (**K**) ($n=4$). (**L**) Lactate level in LOX1$^+$ PMN-MDSCs between NNB and FDNB groups ($n=5$). (**M**) Quantitative real-time PCR (qRT-PCR) of DNA precipitated via chromatin immunoprecipitation (ChIP) with anti-HIF-1α antibody for binding to *S100A8*, *S100A9*, *ARG1*, *LDHA*, and *SLC16A3* promoters in LOX1$^+$ PMN-MDSCs between NNB and FDNB groups ($n=4$). Data are pooled from two independent experiments; *$P<0.05$; **$P<0.01$; ***$P<0.001$; ****$P<0.0001$. Bar graphs show the mean ± SEM. Statistical significance was determined using a two-tailed unpaired Student's t-test (**E, G**, and **J-M**)

(CCA) [46–48]. We firstly evaluated classical HIE models and found that the survival rate of mice after CCA surgery was significantly low, with subjects failing to survive beyond 24 h (Fig. S9A). In contrast, the survival rate of mice in the hypoxia model was markedly improved. Notably, this model effectively simulates fetal intrauterine distress within a clinical context. Consequently, we opted to employ a mouse model exhibiting acute hypoxia in subsequent experiments. The hypoxia model for newborn mice (HNB) were categorized into multiple groups based on various time points following hypoxia, whereas the control newborn mice (CNB) were designated as the control group (Fig. 3A). To examine alterations in brain injury among newborn mice at different post-hypoxia intervals, we assessed the disease phenotypes of brain tissues from healthy newborn mice (0 h) and those subjected to hypoxia at 12, 24, 48, and 72 h post-exposure (Fig. 3A). First, TTC staining revealed a significant infarct in the brains of mice subjected to hypoxia compared to the 0-hour group (Fig. 3B, S9B). Subsequently, both brain water content and geotaxis reflex time in the 24-hour hypoxia group were markedly elevated relative to the 0-hour group, thereby confirming the successful establishment of the hypoxic brain injury model (Fig. 3C, D). The results of H&E and Nissl staining indicated that neuronal damage in the hippocampal regions significantly increased at various time points following hypoxia compared to the 0-hour group. Notably, neuronal damage in the hippocampus peaked at 24 h post-hypoxia, with a marked decline observed 48 h after exposure to hypoxic conditions (Fig. 3E, S9C). Next, NeuN-TUNEL staining revealed a substantial increase in the percent of TUNEL-positive cells and the number of NeuN-TUNEL-positive neurons within the hippocampus following hypoxia relative to the 0-h group, peaking at 24 h and showing a trend toward recovery by 48 h post-hypoxia (Fig. 3F, G; S9D). To investigate the activation of microglial cells in this process, we performed dual immunofluorescent staining for IBA1 and CD68 in the hippocampal region. Our findings indicated that the number of CD68$^+$ IBA1$^+$ double positive microglia cells within the hippocampus following hypoxia, was significantly greater compared to the 0-hour group. This increase peaked at 24 h and exhibited a trend toward recovery by 48 h post-hypoxia (Fig. 3H; S9E). These results demonstrate varying degrees of brain injury at different time intervals after hypoxia and highlight the involvement of activated microglia in this process. Specifically, 12 and 24 h post-hypoxia demonstrated exacerbation of brain injury, whereas 48 and 72 h post-hypoxia indicated remission of the condition.

Given the critical roles of microglia and macrophages in mediating brain tissue injury and regulating inflammation following hypoxia, we first evaluated the proportions of CD11b$^+$CD45^{low} and CD11b$^+$CD45^{high} cells within the brain. The findings revealed no obviously significant changes in the proportions of CD11b$^+$CD45^{low} and CD11b$^+$CD45^{high} cells at various time points post-hypoxia compared with the 0-hour group (Figs. S10A, B). Subsequently, we assessed the expression levels of several inflammation-associated markers and transcription factors, specifically CD80, CD86, CD206, STAT1, and NF-κB within these cells. The results indicated that the expression of CD80 or CD86 exhibited a trend change in CD11b$^+$CD45^{low} cells (Fig. S10C, D); notably, there was an increase at 12 h post-hypoxia, followed by a decrease at 48 h post-hypoxia, compared to 0 h (Fig. S10C, D). Funthermore, flow cytometric results revealed an increase in CD206 surface marker expression following 48-hour hypoxic exposure compared to 0 hour (Fig. S10C, D). In contrast, no changes were observed in CD11b$^+$CD45^{high} cells (Fig. S10C–F). Importantly, the ratios of CD80/CD206 and CD86/CD206 within the CD11b$^+$CD45^{low} population demonstrated a significant changing trend; marked increases were noted at 12 h after hypoxia, followed by substantial decreases at 48 h after hypoxia (Fig. 3I, J). However, this pattern was not observed in CD11b$^+$CD45^{high} cells (Fig. S10G). In both groups examined, the variations in the phosphorylation levels of the transcription factors STAT1 and NF-κB (including p-STAT1, pNF-κB-Thr254, and pNF-κB-Ser529) were consistent with the changes in the ratios of CD80/CD206 to CD86/CD206 in CD11b$^+$CD45^{low} microglia cells rather than CD11b$^+$CD45^{high} cells (Fig. 3K, S10H–J). These findings suggest that microglia characterized as CD11b$^+$CD45^{low} may play a crucial role in hypoxic

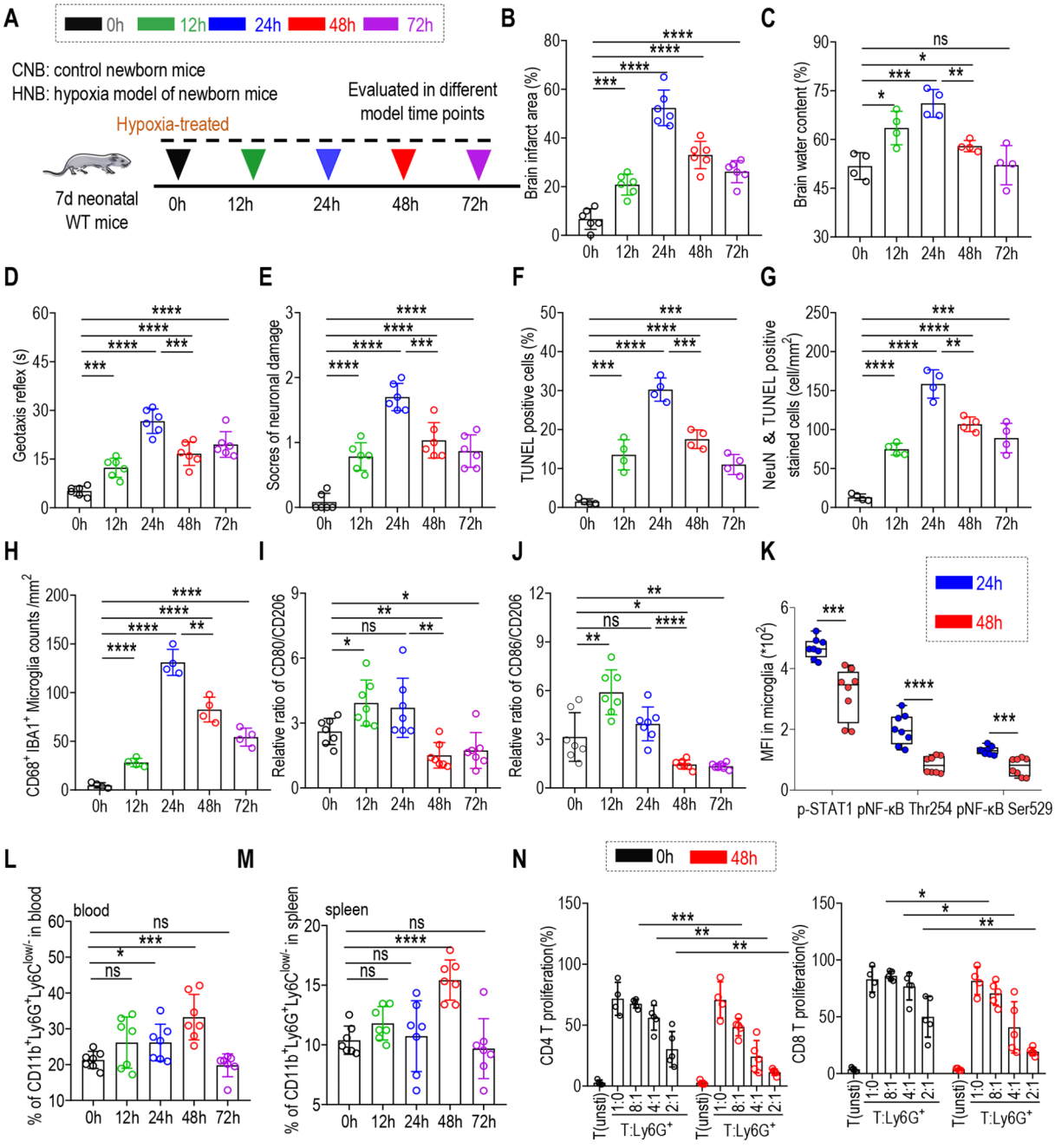

Fig. 3 Enhanced activation of splenic PMN-MDSCs alleviates brain injury and reduces microglial activation and inflammatory factor expression. (**A**) Strategy of the hypoxia model of 7-day-old neonate mice. (**B**) Statistical analysis of the percentage of brain infarct area at different periods of CNB and HNB ($n=6$). (**C**) Statistical analysis of brain water content results in the brain at different periods of CNB and HNB ($n=4$). (**D**) Statistical analysis of geotaxis reflex time in the brain at different periods of CNB and HNB ($n=4$). (**E-H**) Statistical analysis of hippocampal neuronal damage scores ($n=6$) (**E**), the percentage of TUNEL cells ($n=4$) (**F**), the number of NeuN-TUNEL positive mouse hippocampal neurons ($n=4$) (**G**), the counts of $CD68^+$ $IBA1^+$ double positive microglia cells within the hippocampal ($n=4$) (**H**) at different periods of control newborn mice (CNB) and hypoxia models of newborn mice (HNB). (**I, J**) Statistical analysis of CD80/CD206 and CD86/CD206 relative ratios at different periods after hypoxia ($n=7$). (**K**) Statistical analysis of p-STAT1, pNF-κB Thr254, and pNF-κB Ser529 levels in $CD11b^+$ $CD45^{low}$ microglia at 24 h and 48 h after hypoxia ($n=8$). (**L, M**) Representative Statistical analysis of PMN-MDSCs in the spleen and blood from neonate mice at different periods after hypoxia ($n=7$). (**N**) Statistical analysis of the proliferation rates of $CD4^+$ T cells and $CD8^+$ T cells from CNB and HNB groups. $CD3^+$ T cells isolated from BALB/c mouse spleen were cocultured with $Ly6G^+$ PMN-MDSCs stimulated with Con A at different ratios for 72 h, and the proliferation of T cells was examined by CFSE staining; unstimulated T cells were used as a negative control ($n=4$). Data are pooled from two independent experiments; $^*P<0.05$; $^{**}P<0.01$; $^{***}P<0.001$; $^{****}P<0.0001$. Bar graphs show the mean ± SEM. Statistical significance was determined using a two-tailed unpaired Student's t-test (**B-N**)

conditions, whereas peripheral infiltrated macrophages as well as activated microglia identified as $CD11b^{+}CD45^{high}$ do not exhibit similar responses.

Additionally, the numbers of MDSCs and their subsets in the brains of newborn mice were assessed following hypoxia. The data indicated no significant alterations in the proportions of PMN-MDSCs, M-MDSCs, or total MDSCs in the brain at various time points compared to the 0 h group (Fig. S11A-E). Subsequently, we evaluated the levels of PMN-MDSCs and M-MDSCs in both the spleen and whole blood of newborn mice after hypoxia. Our findings demonstrated a significant increase in the proportion of PMN-MDSCs within both the spleen and whole blood at 48 h after hypoxia, relative to the 0-hour group (Fig. 3L, M). However, no significant changes were observed in the proportion of M-MDSCs at any of the time points (Fig. S11F-I). Furthermore, we examined the function of splenic PMN-MDSCs from CNB and HNB, and the results demonstrated a significant decrease in the proliferation rates of $CD4^{+}$ and $CD8^{+}$ T cells in HNB compared to those in CNB, indicating an enhanced immunosuppressive function of PMN-MDSCs in newborn mice after hypoxia (Fig. 3N, S12A). These findings suggest that the expression of inflammatory factors in brain microglia occurs initially, followed by a subsequent increase in the activation of peripheral PMN-MDSCs after hypoxia in newborn mice.

Depletion of PMN-MDSCs worsened brain injury, increasing microglial activation and inflammatory factor expression

To demonstrate the correlation between the activation of peripheral PMN-MDSCs and the expression of inflammatory factors in brain microglia after hypoxia, we conducted a clearance experiment on PMN-MDSCs before hypoxia. An intraperitoneal injection of Ly6G antibody was used to clear the PMN-MDSCs, with IgG antibody used as the control group (Fig. S13A). As expected, the results showed a significant decrease in the proportion of PMN-MDSCs in the spleen and whole blood in the Ly6G antibody group compared to those in the IgG group, as well as in the proportion of M-MDSCs, confirming the successful in vivo clearance of peripheral PMN-MDSCs (Fig. S13B-E). The results show increased infarction area (Fig. 4A, S13F), elevated brain water content (Fig. 4B), and prolonged geotaxis reflex time (Fig. 4C) after PMN-MDSC depletion. Furthermore, analyses using H&E and Nissl staining revealed a significant increase in neuronal damage within the hippocampus of newborn mice treated with the Ly6G mAb compared to those treated with IgG2b mAb (Fig. 4D-F). Additionally, the NeuN-TUNEL staining results demonstrated a marked increase in the percent of TUNEL-positive cells and the number of NeuN-TUNEL-positive neurons within the hippocampus of newborn mice in the Ly6G mAb group relative to those in the IgG2b mAb group (Fig. 4G, H). In addition, an increase number of $CD68^{+}$ $IBA1^{+}$ double positive microglia cells within the hippocampus were observed in the Ly6G mAb group compared to the IgG2b mAb group (Fig. 4I, J, S13G). These findings indicate that the depletion of PMN-MDSCs exacerbates brain injury in newborns, which is accompanied by enhanced microglial activation. Subsequently, the proportions of $CD11b^{+}CD45^{low}$ and $CD11b^{+}CD45^{high}$ cells in the brain and the expression levels of inflammatory factors within these cells were evaluated (Fig. S13H-L). These findings were consistent with those observed in neonatal mice at various time points following hypoxia, indicating that only $CD11b^{+}CD45^{low}$ microglia were involved (Fig. S13H-L). Notably, compared to the IgG2b mAb antibody group, there was a significant increase in the ratio of CD80/CD206 and CD86/CD206 and elevated phosphorylation levels of transcription factors STAT1 and NF-κB in brain $CD11b^{+}CD45^{low}$ microglia from hypoxic newborn mice treated with Ly6G mAb group (Fig. 4K, L), while no change was observed in $CD11b^{+}CD45^{high}$ cells (Fig. S13K, L). These results suggest that activation of peripheral PMN-MDSCs plays a critical role in regulating inflammation mediated by $CD11b^{+}CD45^{low}$ microglia.

HIF-1α in neonatal mouse PMN-MDSCs plays a crucial role in mitigating brain injury following acute hypoxia

Similar to the clinical results, we initially assessed the mRNA changes in HIF family genes and found no differences among the three time points (0, 24, and 48 h) (Fig. S14A). However, we observed varying degrees of accumulation of HIF-1α protein at different time points in neonatal mice under hypoxia, rather than HIF-2α or HIF-1β levels (Fig. 5A-C). In line with previous clinical observations, further in vitro experiments revealed that the proteasome inhibitor MG132 significantly enhanced the stability of HIF-1α protein (Fig. S14B). To more precisely elucidate the role of HIF-1α in neonatal PMN-MDSCs, $HIF\text{-}1\alpha^{fl/fl}$ mice were crossed with $S100A8^{cre}$ mice to achieve specific deletion of HIF-1α in PMN-MDSCs. This resulted in the generation of $HIF\text{-}1\alpha^{fl/fl}$ $S100A8^{cre}$ mice, and genotyping confirmation was performed using PCR to verify the expression of HIF-1α and S100A8 alleles (Fig. S15A). The efficiency of HIF-1α gene knockout in mice was also evaluated. The data indicated a significant downregulation of HIF-1α expression in PMN-MDSCs, both at the mRNA and protein levels (Fig. S15B, C). Subsequently, we measured the body weights of the mice and observed no discernible differences under physiological conditions (Fig. S15D). Given that hypoxia increases the risk of neurological dysfunction, we examined the effects of HIF-1α deficiency in newborn mice through behavioral tests conducted under

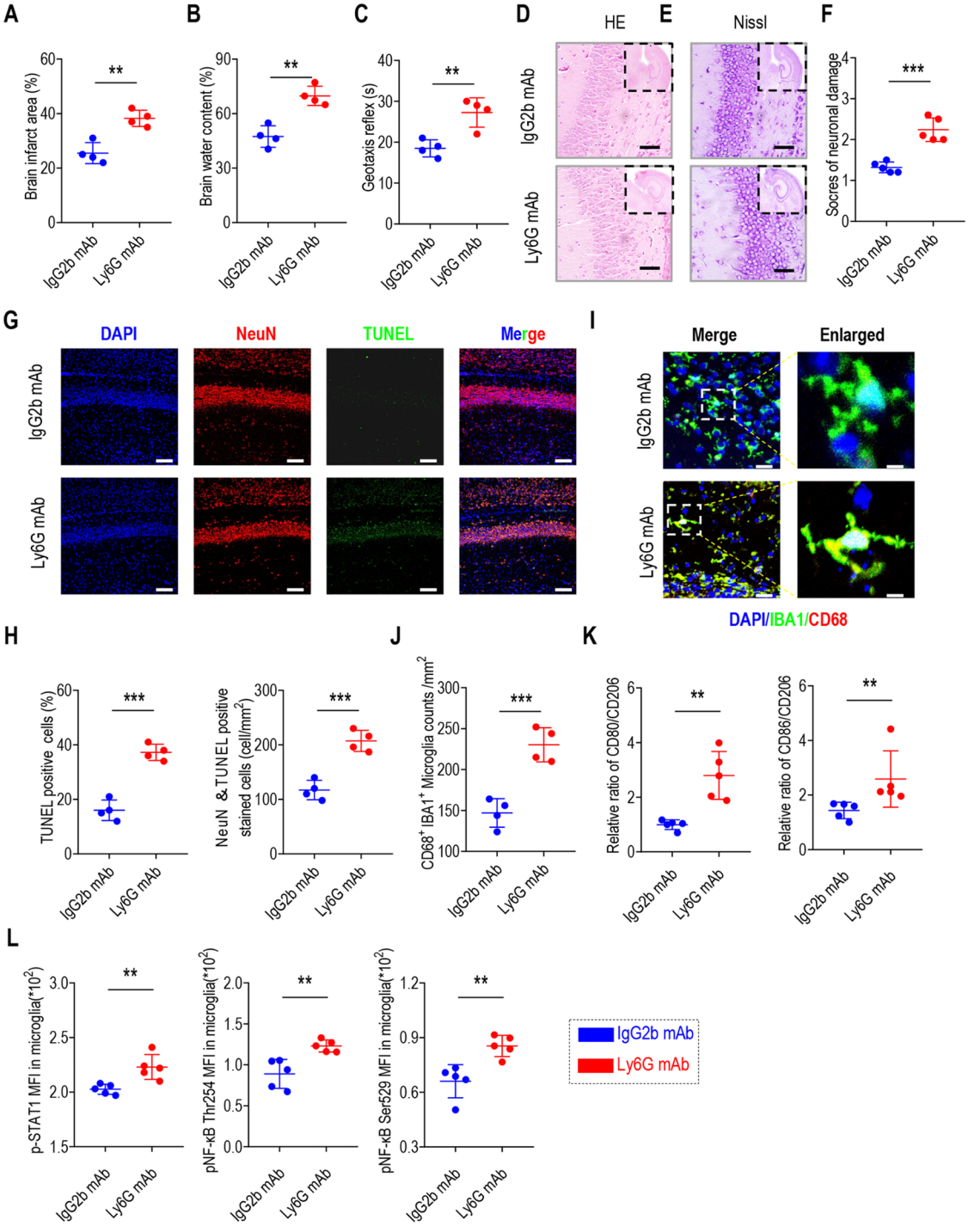

Fig. 4 (See legend on next page.)

(See figure on previous page.)

Fig. 4 Depletion of PMN-MDSCs worsened brain injury, increasing microglial activation and inflammatory factor expression. PMN-MDSC depletion in hypoxia model of 7-day-old mice model to analysis (**A–L**): (**A**) Statistical analysis of the percentage of brain infarct area in Ly6G mAb group and IgG2b mAb group ($n=4$). (**B**) Statistical analysis of brain water content results in Ly6G mAb group and IgG2b mAb group ($n=4$). (**C**) Statistical analysis of geotaxis reflex time in Ly6G mAb group and IgG2b mAb group ($n=4$). (**D**) Representative HE staining image (original magnification, ×400) in IgG and Ly6G antibody groups. (**E**) Representative Nissl staining image (original magnification, ×400) and (**F**) statistical analysis of the hippocampal neuronal damage scores in Ly6G mAb group and IgG2b mAb group ($n=5$). (**G**) Representative images of NeuN (red) and TUNEL staining (green) in the hippocampal region and DAPI staining is shown in blue. Scale bar = 50 μm. (**H**) Statistical analysis of the percentage of TUNEL cells and the number of NeuN-TUNEL positive mouse hippocampal neurons in Ly6G mAb group and IgG2b mAb group ($n=4$). (**I**) Representative merged and enlarged images showing CD68, IBA1, and DAPI co-staining in the hippocampus (Scale bar = 50 μm). (**J**) Statistical analysis of the number of $CD68^+$ $IBA1^+$ double positive microglia cells within the hippocampal for Ly6G mAb group and IgG2b mAb group ($n=4$). (**K**) Statistical analysis of CD80/CD206 and CD86/CD206 relative ratios in Ly6G mAb group and IgG2b mAb group ($n=5$). (**L**) Statistical analysis of p-STAT1, pNF-κB Thr254, and pNF-κB Ser529 levels in microglia from Ly6G mAb group and IgG2b mAb group ($n=5$). Data are pooled from two independent experiments; $^*P<0.05$; $^{**}P<0.01$; $^{***}P<0.001$; $^{****}P<0.0001$. Bar graphs show the mean ± SEM. Statistical significance was determined using a two-tailed unpaired Student's t-test (**A- C, F, H, J - L**)

physiological conditions. The results demonstrated that the absence of HIF-1α in PMN-MDSCs did not impair motor abilities in newborn mice, as evidenced by comparable performance in walking, hindlimb strength, as well as prolonged surface righting and negative geotaxis walk latencies (Fig. S15E). We also investigated whether the conditional loss of HIF-1α under physiological conditions would influence the severity of brain injury. Data indicated that there were no significant changes in infarct area, brain water content, or geotaxis reflex time (Fig. S16A-C). Additionally, parameters such as neuronal damage in the hippocampus as evidenced by H&E and Nissl staining, the percentage of TUNEL-positive cells, the number of NeuN-TUNEL-positive neurons within the hippocampus, and the number of $CD68^+$ $IBA1^+$ double positive microglial cells in the hippocampus showed no differences when comparing the HIF-$1\alpha^{fl/fl}$ $S100A8^{cre}$ mice to the HIF-$1\alpha^{fl/fl}$mice (Fig. S16D-G). Furthermore, there were no observed alterations in the proportions of $CD11b^+CD45^{low}$-expressing microglia and $CD11b^+CD45^{high}$-expressing cells, the proportions of CD80 or CD86 or CD206, the relative ratios of CD80/CD206 and CD86/CD206, nor in the phosphorylation level of STAT1 and NF-κB within $CD11b^+CD45^{low}$ and $CD11b^+CD45^{high}$ cells in the brain (Fig. S16H, I). Collectively, these findings underscore that a lack of HIF-1α under physiological conditions does not impact neonatal brain injury.

Subsequently, we conducted acute hypoxia modeling in knockout mice by dividing 7-day-old neonatal mice into two groups: the HIF-$1\alpha^{fl/fl}$ group and the HIF-$1\alpha^{fl/fl}$ $S100A8^{cre}$ group (Fig. S17A). Notably, the knockout of HIF-1α in PMN-MDSCs led to an exacerbation of brain injury, as evidenced by several observations. An increased area of brain infarction (Fig. 5D, S17B), elevated brain water content (Fig. 5E), prolonged geotaxis reflex time (Fig. 5F), and heightened neuronal damage in the hippocampus demonstrated through H&E and Nissl staining (Fig. 5G-I) were all noted. Additionally, there was a rise in the percentage of TUNEL-positive cells and an increase in the number of NeuN-TUNEL-positive neurons within the hippocampus (Fig. 5J, K). Furthermore, a significant increased number of $CD68^+$ $IBA1^+$ double positive microglia cells within the hippocampus was observed (Fig. 5L, M, S17C). The proportions of $CD11b^+CD45^{low}$ and $CD11b^+CD45^{high}$ cells in the brain and the expression levels of inflammatory factors among those cells were also assessed. Results are consistent with those observed for the clearance of PMN-MDSCs in neonatal mice, revealing that only $CD11b^+CD45^{low}$ microglia, rather than $CD11b^+CD45^{high}$ cells, are involved (Fig. S17D, E). Notably, compared to the HIF-$1\alpha^{fl/fl}$ group, there was a significant increase in the ratio of CD80/CD206 and CD86/CD206 and elevated phosphorylation levels of transcription factors STAT1 and NF-κB in the $CD11b^+CD45^{low}$ microglia from HIF-$1\alpha^{fl/fl}S100A8^{Cre}$ group mice after hypoxia (Fig. 5N, O), whereas no obviously change was observed in $CD11b^+CD45^{high}$ cells (Fig. S17E). These results underscore that HIF-1α expression in PMN-MDSCs plays a critical role in regulating inflammation mediated by brain $CD11b^+CD45^{low}$ microglia.

PMN-MDSCs from HIF-1α deficient mice exhibit reduced brain injury mitigation, with heightened microglia activation and inflammatory factor expression

Based on the above observations, we next investigated the potential therapeutic value of HIF-1α of PMN-MDSCs in neonatal inflammation. Splenic PMN-MDSCs were sorted from acute hypoxia treated 7-d-old HIF-$1\alpha^{fl/fl}$ or HIF-$1\alpha^{fl/fl}$ $S100A8^{cre}$ neonatal mice and adoptively transferred into recipient mice (WT 7-d neonatal mice) 1 h before the induction of hypoxia (Fig. S18A). The results indicated that the adoptive transfer of PMN-MDSCs from HIF-$1\alpha^{fl/fl}$ $S100A8^{cre}$ neonatal mice significantly exacerbated the severity of brain injury (Fig. 6A–L). This was evidenced by an enlarged brain infarct area (Fig. 6A, S18B), as demonstrated by TTC staining, increased brain water content (Fig. 6B), and prolonged geotaxis reflex time (Fig. 6C). Additionally, H&E and Nissl staining revealed a significant increase in neuronal damage within the hippocampus (Fig. 6D-F). TUNEL assays further indicated a notable rise in the percentage of TUNEL-positive cells and the number of NeuN-TUNEL-positive neurons within the hippocampus (Fig. 6G, H). This was

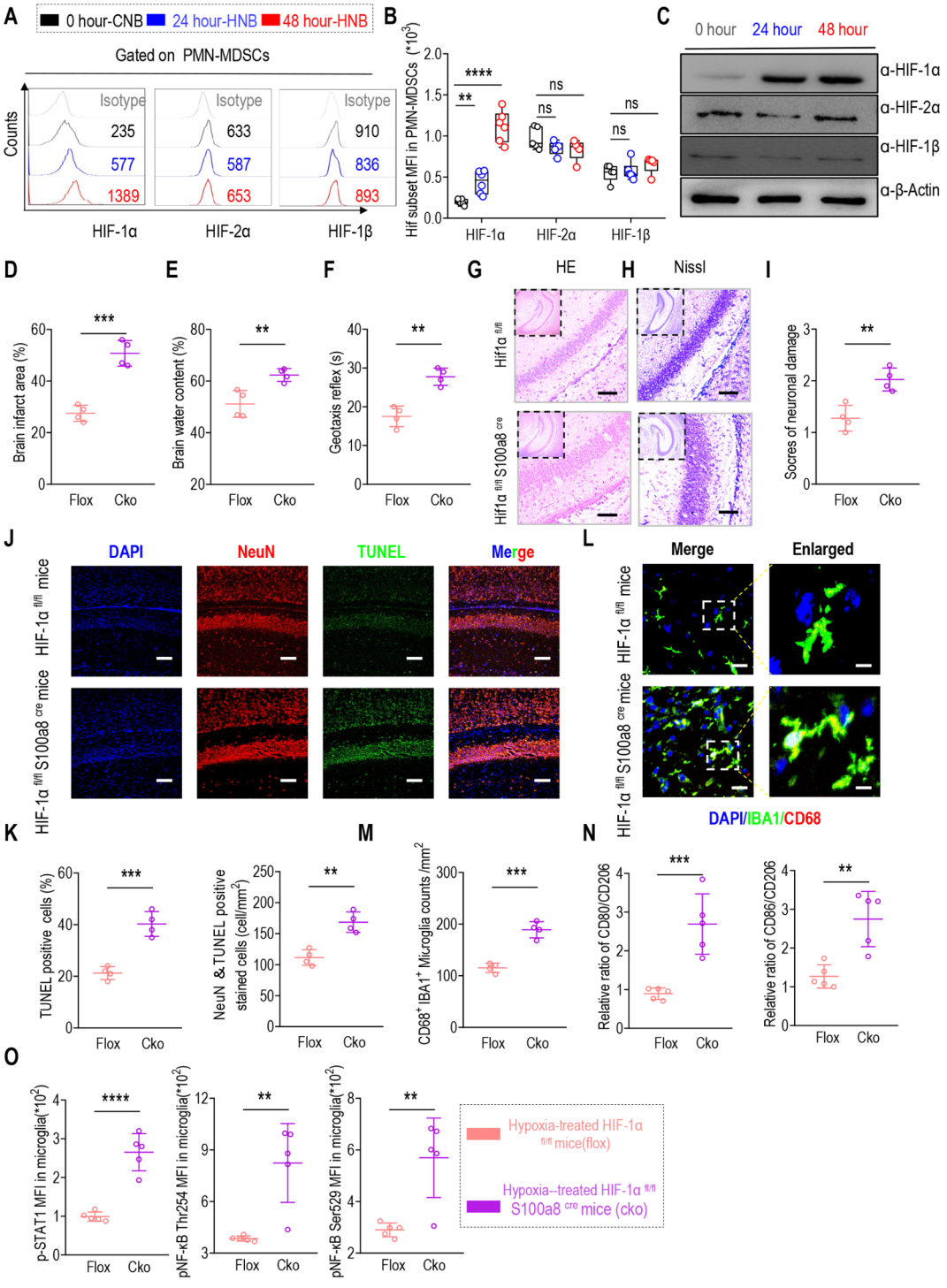

Fig. 5 (See legend on next page.)

(See figure on previous page.)

Fig. 5 HIF-1α in neonatal mouse PMN-MDSCs plays a crucial role in mitigating brain injury following acute hypoxia. (**A** and **B**) Representative flow cytometry results (left) and statistical analysis (right) of HIF-1α ($n=6$), HIF-2α ($n=5$), and HIF-1β level ($n=5$) in PMN-MDSCs from 0-h-NNB, 24-h-HNB, and 48-h-HNB mice. (**C**) PMN-MDSCs sorted from 0-h-NNB, 24-h-HNB, and 48-h-HNB spleens in mice to analyze the protein levels of HIF-1α, HIF-2α, and HIF-1β by western blotting experiment. Hypoxia model of 7-day-old mice in HIF-1α deficiency in PMN-MDSC to analysis (**D–O**): (**D**) Statistical analysis of the percentage of brain infarct area in HIF-1α$^{fl/fl}$ mice and HIF-1α$^{fl/fl}$ S100A8^{cre} mice groups after hypoxia treatment ($n=4$). (**E**) Statistical analysis of brain water content results in the brain in HIF-1α$^{fl/fl}$ mice and HIF-1α$^{fl/fl}$ S100A8^{cre} mice groups ($n=4$). (**F**) Statistical analysis of geotaxis reflex time in the brain in HIF-1α$^{fl/fl}$ mice and HIF-1α$^{fl/fl}$ S100A8^{cre} mice groups ($n=4$). (**G**) Representative H&E staining image (original magnification, ×400) in HIF-1α$^{fl/fl}$ mice and HIF-1α$^{fl/fl}$ S100A8^{cre} mice groups. (**H**) Representative Nissl staining image (original magnification, ×400) and (**I**) statistical analysis of the hippocampal neuronal damage scores in HIF-1α$^{fl/fl}$ mice and HIF-1α$^{fl/fl}$ S100A8^{cre} mice groups ($n=4$). (**J**) Representative images of NeuN (red) and TUNEL staining (green) in the hippocampal region and DAPI staining is shown in blue. Scale bar = 50 μm. (**K**) Statistical analysis of the percentage of TUNEL cells and the number of NeuN-TUNEL positive mouse hippocampal neurons in HIF-1α$^{fl/fl}$ mice and HIF-1α$^{fl/fl}$ S100A8^{cre} mice groups ($n=4$). (**L**) Representative merged and enlarged images showing CD68, IBA1, and DAPI co-staining in the hippocampus (Scale bar = 50 μm). (**M**) Statistical analysis of the number of CD68^{+} IBA1^{+} double positive microglia cells within the hippocampal for HIF-1α$^{fl/fl}$ mice and HIF-1α$^{fl/fl}$ S100A8^{cre} mice groups ($n=4$). (**N**) Statistical analysis of CD80/CD206 and CD86/CD206 relative ratios in HIF-1α$^{fl/fl}$ mice and HIF-1α$^{fl/fl}$ S100A8^{cre} mice groups ($n=5$). (**O**) Statistical analysis of p-STAT1, pNF-κB Thr254 and pNF-κB Ser529 levels in microglia from HIF-1α$^{fl/fl}$ mice and HIF-1α$^{fl/fl}$ S100A8^{cre} mice groups ($n=5$). Bar graphs show the mean ± SEM. Statistical significance was determined using a two-tailed unpaired Student's *t*-test (**B, D-F, I, K**, and **M-O**)

accompanied by an elevated number of CD68^{+} IBA1^{+} double positive microglia cells within the hippocampus, as demonstrated through Immunofuorescence staining (Fig. 6I, J, S18C). Compared to the transfer of PMN-MDSCs from HIF-1α$^{fl/fl}$ neonatal mice, the transfer of PMN-MDSCs from HIF-1α$^{fl/fl}$ S100A8^{cre} neonatal mice led to a significant increase in the ratios of CD80/CD206 and CD86/CD206 (Fig. 6K, S18D). Additionally, there were elevated phosphorylation levels of the transcription factors STAT1 and NF-κB within the CD11b^{+}CD45^{low} microglia (Fig. 6L). In contrast, no effects on these parameters were observed in CD11b^{+}CD45^{high} cells (Fig. S18E). These findings underscore the critical role of HIF-1α in PMN-MDSCs for regulating inflammation following hypoxia in newborn mice.

Lactate transport mediated by HIF-1α serves as a primary factor in mitigating brain injury

To identify the regulatory mechanisms, PMN-MDSCs from the CNB (0 h) and HNB (24 and 48 h) groups were collected for subsequent analyses. First, the upregulated PMN-MDSC-related target genes (S100a8, S100a9, Arg1, Cox2) were identified after hypoxic treatment (Fig. 7A). Consistent with the human data, the expression of S100a9, Arg1, and Cox2 in PMN-MDSCs, the mean fluorescence intensity (MFI) of S100a9, arginase activity, and PGE2 production from the HNB group was significantly higher than that in PMN-MDSCs from the CNB group (Fig. 7B-E). Besides, up-regulation of genes involved in glycolysis process (*Pfkfb2*, *Pfkfb3*, *Pfkfb4*, *Gpi*, *Aldoa*, *Aldoc*, *Pkm*, *Ldha*) and lactate transporter (*slc16a3*) was detected at the mRNA level (Fig. 7F), whereas no change was observed in other lactate transporter (*Gpr81 and Slc16a1*) (Fig. S19A). Consistent with human findings, the HNB group exhibited an increase in ECAR and a comparable, albeit minor, alteration in OCR compared to the CNB group (Fig. 7G-I; Fig. S20A, B). More importantly, increased secretion of lactate (Fig. 7J) and enhanced binding capacity of the HIF-1α protein to the genes (including *S100a8*, *S100a9*, *Arg1*, *Ldha*, and *Slc16a3*) in mouse PMN-MDSCs from the HNB group was also observed (Fig. 7K, S21A, B). The observations indicate that HIF-1α enhances the expression of glycolysis-related genes in PMN-MDSCs of the HNB group.

However, the deletion of HIF-1α in PMN-MDSCs worsened brain injury, accompanied by a reversal in glycolysis metabolism, lactate level, and the binding capacity of HIF-1α (Fig. 7L–Q). Specifically, the expression levels of PMN-MDSCs-related target genes (*S100a8*, *S100a9*, *Arg1*, *Cox2*) and genes involved in glycolysis (*Pfkfb2*, *Pfkfb3*, *Pfkfb4*, *Gpi*, *Aldoa*, *Aldoc*, *Pkm2*, *Ldha*) and lactate transporter (*slc16a3*) decreased significantly in the HIF-1α$^{fl/fl}$ S100A8^{cre} mice hypoxia-treated group compared to in the HIF-1α$^{fl/fl}$ mice hypoxia-treated group (Fig. 7L, S22A, B). The ECAR results also demonstrated increased glycolysis and enhanced glycolytic capacity in HIF-1α$^{fl/fl}$ mice, yet HIF-1α$^{fl/fl}$ S100A8^{cre} mice exhibited lower metabolic activity after acute hypoxia treatment (Fig. 7M-O). Besides, lactate level (Fig. 7P) decreased in PMN-MDSCs from HIF-1α$^{fl/fl}$ S100A8^{cre} mice significantly. Similarly, weakened binding capacity to the above genes, including *S100a8*, *S100a9*, *Arg1*, *Ldha*, and *Slc16a3* was observed in HIF-1α$^{fl/fl}$ S100A8^{cre} mice than in HIF-1α$^{fl/fl}$ mice owing to the ablation of HIF-1α in PMN-MDSCs (Fig. 7Q). Overall, HIF-1α-mediated glycolysis and lactate transport potentially plays a significant role in acute brain injury.

Lactate from PMN-MDSCs significantly reduces brain injury by decreasing microglial activation and inflammatory factor expression

Lactate, an energy source and signaling molecule that plays an important role in inflammation, can cross the blood-brain barrier (BBB) to meet the energy requirements of neurons [61–63]. Lactate modulates immune responses and inflammatory states by activating signaling pathways, altering epigenetic processes and mediating post-translational modifications in the immune system [64, 65]. Owing to their potential role in the regulation

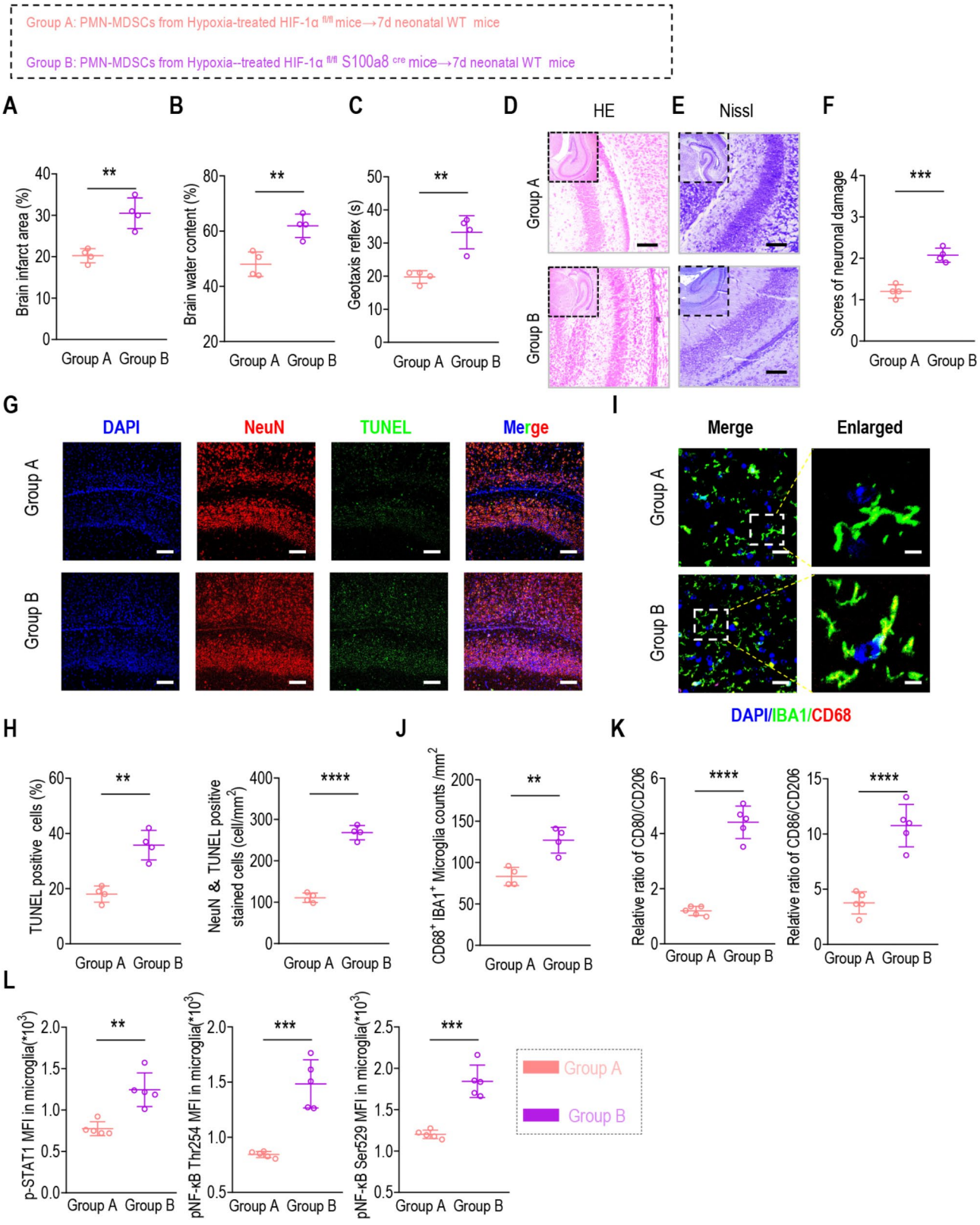

Fig. 6 (See legend on next page.)

(See figure on previous page.)

Fig. 6 PMN-MDSCs from HIF-1α deficient mice exhibit reduced brain injury mitigation, with heightened microglia activation and inflammatory factor expression. Adoptive transfers experiment from 7-day-old mice in HIF-1α deficiency mice to analysis (**A–L**): (**A**) statistical analysis of the percentage of brain infarct area in adoptive transfer assay for PMN-MDSCs from hypoxia-treated HIF-1α$^{fl/fl}$ mice and HIF-1α$^{fl/fl}$ S100A8^{cre} mice. (**B**) Statistical analysis of brain water content results in adoptive transfer assay ($n=4$). (**C**) Statistical analysis of geotaxis reflex time in adoptive transfer assay ($n=4$). (**D**) Representative H&E staining image (original magnification, ×400) in adoptive transfer assay. (**E**) Representative Nissl staining image (original magnification, ×400) and (**F**) statistical analysis of the hippocampal neuronal damage scores in adoptive transfer assay ($n=4$). (**G**) Representative images of NeuN (red) and TUNEL staining (green) in the hippocampal region and DAPI staining is shown in blue. Scale bar = 50 μm. (**H**) Statistical analysis of the percentage of TUNEL cells and the number of NeuN-TUNEL positive mouse hippocampal neurons in adoptive transfer assay ($n=4$). (**I**) Representative merged and enlarged images showing CD68, IBA1, and DAPI co-staining in the hippocampus (Scale bar = 50 μm). (**J**) Statistical analysis of the counts of CD68$^+$ IBA1$^+$ double positive microglia cells within the hippocampal for adoptive transfer assay ($n=4$). (**K** and **L**) Statistical analysis of CD80/CD206 and CD86/CD206 relative ratios (**K**), p-STAT1, pNF-κB Thr254 and pNF-κB Ser529 levels of CD11b$^+$ CD45^{low} microglia (**L**) ($n=5$). Data were pooled from two independent experiments; $^*P<0.05$, $^{**}P<0.01$, $^{***}P<0.001$, and $^{****}P<0.0001$. Bar graphs show the mean ± SEM. Statistical significance was determined using a two-tailed unpaired Student's *t*-test (**A-C, F, H**, and **J-L**)

of immune and inflammatory processes, we hypothesized that lactate derived from PMN-MDSCs is involved in the regulation of microglial inflammatory responses after acute hypoxia in neonatal mice. We therefore performed acute hypoxia modelling in knockout mice, dividing 7-day-old neonatal mice into two groups: HIF-1α$^{fl/fl}$ S100A8^{cre} mice group, HIF-1α$^{fl/fl}$ S100A8^{cre} mice + Lactate group. In the intervention experiments, 2 g/kg lactate was injected into mice intraperitoneally for 2 consecutive days, and brain pathology was evaluated 48 h after hypoxia (Fig. S23A). The data indicated that lactate injection significantly alleviated brain injury, as evidenced by the following observations: a reduction in the brain infarct area (Fig. 8A; S23B), a diminished brain water content (Fig. 8B), a lessened geotaxis reflex time (Fig. 8C). H&E and Nissl staining results demonstrating a marked decrease in neuronal damage within the hippocampus of both CA and GA regions (Fig. 8D–F), and TUNEL assay results showing a significant reduction in percent of TUNEL-positive cells and number of NeuN-TUNEL-positive neurons within the hippocampus (Fig. 8G, H), as well as the dropped number of CD68$^+$ IBA1$^+$ double positive microglia cells within the hippocampus by immunostaining staining (Fig. 8I, J, S23C). Collectively, these pathological findings suggest that lactate supplementation substantially reversed hypoxic brain damage in HIF-1α$^{fl/fl}$S100A8^{cre} mice. Furthermore, the ratios of CD80/CD206 and CD86/CD206, along with the phosphorylation levels of transcription factors STAT1 and NF-κB, were significantly reduced in brain CD11b$^+$CD45^{low} microglia from HIF-1α$^{fl/fl}$S100A8^{cre} neonatal mice treated with lactate compared to those from untreated HIF-1α$^{fl/fl}$S100A8^{cre} neonatal mice (Fig. 8K-L, S23D). This reduction was not observed in CD11b$^+$CD45^{high} cells from the brains of HIF-1α$^{fl/fl}$S100A8^{cre} neonatal mice treated with lactate (Fig. S23E). Taken together, these results indicated that lactate plays a protective role against neuroinflammation associated with brain injury following hypoxia in neonatal mice.

To further elucidate the direct effects of lactate on microglia, we introduced lactate into sorted brain microglia within an in vitro culture system and incubated them for 72 h. The results indicated that, compared to microglia cultured alone, the ratios of CD80/CD206 and CD86/CD206 were significantly reduced when co-cultured with lactate (Fig. 8M). Subsequently, we employed various microglial cell lines, including both the mouse microglial cell line BV2 and the human microglial cell line HMC3, in our co-culture system; these findings were consistent with those observed in microglia isolated from brain tissue. Specifically, when comparing groups where lactate was co-cultured with microglia to those cultured alone, there was a significant decrease in the ratios of CD80/CD206 and CD86/CD206 among microglial cells (Fig. 8N, O). In summary, lactate released through HIF-1α-mediated glycolysis in PMN-MDSCs directly influenced the expression of inflammatory factors in microglia, thereby contributing to the mitigation of brain injury following neonatal hypoxia.

Discussion

In this study, we examined the role of PMN-MDSCs in hypoxia-induced inflammation and brain injury. Clinical findings showed increased activation and anti-inflammatory signals in PMN-MDSCs from FDNB. Correlation analysis revealed a significant negative relationship between PMN-MDSC levels and the neurological injury marker (NSE). Transcriptomic analysis indicated that HIF-1α mediates glycolytic activation in PMN-MDSCs, leading to lactate production and transport. Animal model results demonstrated that heightened peripheral PMN-MDSC activation in neonatal mice after acute hypoxia was essential for reducing brain damage, showing a time-dependent correlation with the change of microglial activation and inflammatory factor expression. Conditional knockout of HIF-1α confirms its necessity for PMN-MDSC activation after neonatal hypoxia. Mechanistically, following hypoxia, elevated HIF-1α expression in peripheral PMN-MDSCs significantly boosted lactate secretion while downregulating microglial activation and altering the CD80/CD206 and CD86/CD206 ratios. This also reduced phosphorylation levels of transcription factors STAT1 and NF-κB within brain

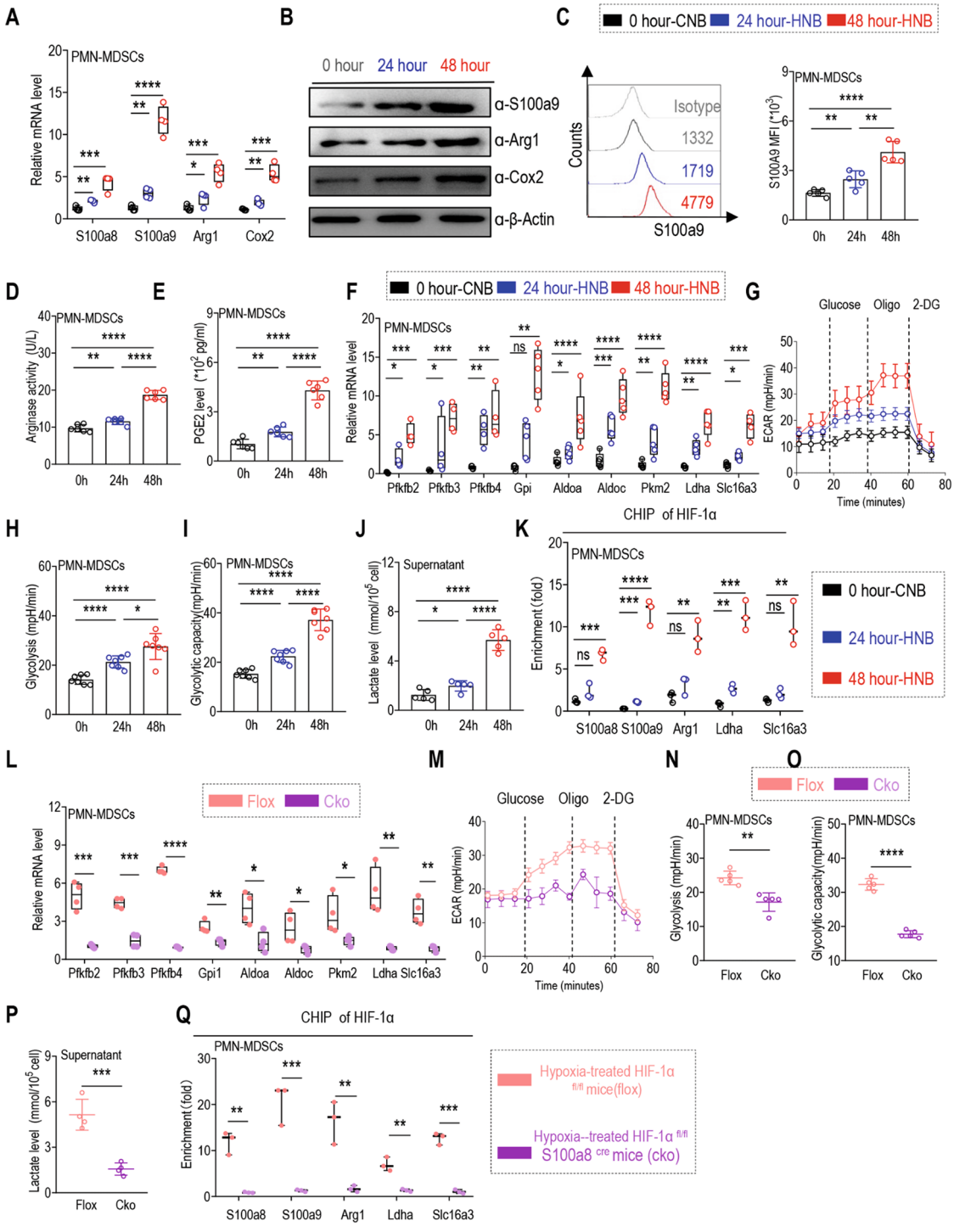

Fig. 7 (See legend on next page.)

(See figure on previous page.)

Fig. 7 Lactate transport mediated by HIF-1α serves as a primary factor in mitigating brain injury. PMN-MDSCs sorted from 0-h-NNB, 24-h-HNB, and 48-h-HNB spleens of mice for analysis (**A-K**): (**A**) mRNA levels of *S100a8*, *S100a9*, *Arg1*, and *Cox2* ($n=4$). (**B**) Protein levels of *S100a9*, *Arg1*, and *Cox2*. (**C**) Representative flow cytometry results (left) and statistical analysis (right) of S100a9 level ($n=5$). (**D**) Arginase activity ($n=6$). (**E**) PGE2 levels ($n=6$). (**F**) mRNA levels of genes involved in glycolysis metabolism (*Pfkfb2*, *Pfkfb3*, *Pfkfb4*, *Gpi*, *Aldoa*, *Aldoc*, *Pkm*, *Ldha*) and lactate transport (*slc16a3*) ($n=4$). (**G-I**) Seahorse analysis of the ECAR curve and glycolysis capacity ($n=7$). (**J**) Lactate levels in the supernatants ($n=5$). (**K**) Quantitative real-time PCR (qRT-PCR) of DNA precipitated via chromatin immunoprecipitation (ChIP) with anti-*HIF-1α* antibody for binding to *S100a8*, *S100a9*, *Arg1*, *Ldha*, and *Slc16a3* promoters ($n=3$). PMN-MDSCs sorted from HIF-1α$^{fl/fl}$ mice and HIF-1α$^{fl/fl}$ S100A8^{cre} mice spleens after acute hypoxia-treated to analysis (**L-Q**): (**L**) mRNA levels of genes involved in glycolysis metabolism (*Pfkfb2*, *Pfkfb3*, *Pfkfb4*, *Gpi*, *Aldoa*, *Aldoc*, *Pkm*, *Ldha*) and lactate transport (*slc16a3*) ($n=4$). (**M-O**) Seahorse analysis of the ECAR curve and glycolysis capacity ($n=5$). (**P**) Lactate levels in the supernatant ($n=4$). (**Q**) Quantitative real-time PCR (qRT-PCR) of DNA precipitated via chromatin immunoprecipitation (ChIP) with anti-*HIF-1α* antibody for binding to *S100a8*, *S100a9*, *Arg1*, *Ldha*, and *Slc16a3* promoters ($n=3$). Data were pooled from two independent experiments; $^{*}P<0.05$, $^{**}P<0.01$, $^{***}P<0.001$, and $^{****}P<0.0001$. Bar graphs show the mean ± SEM. Statistical significance was determined using two-tailed unpaired Student's *t*-test (**A, C-F, H-L**, and **N-Q**)

$CD11b^{+}CD45^{low}$ microglia, thereby alleviating brain damage.

The activation of microglia in response to endogenous stimuli, such as infection or injury, is a hallmark of neuroinflammation [10, 15, 66]. Microglia exhibit dynamic switching based on environmental signals during various stages of the inflammatory response [64, 65]. Our findings showed that inflammatory factor levels in brain microglia were significantly elevated at 12 and 24 h, coinciding with worsened brain injury. A reduction was observed at 48 h, aligning with the alleviation of brain injury after hypoxia. This change correlated closely with enhanced peripheral PMN-MDSC activation. Emerging evidence indicates that MDSCs are involved in regulating neonatal inflammation [24, 25, 45, 57]. This study is the first to demonstrate increased PMN-MDSC activation and anti-inflammatory signal release in acute FDNB, along with a significant negative correlation between PMN-MDSC and NSE levels (neurologic injury markers). RNA-seq results and KEGG/GO analysis revealed that HIF-1α signaling pathway involvement contributes to augmented PMN-MDSC activation in FDNB. Data indicated that HIF-1α levels in PMN-MDSCs significantly increased after 48 h of hypoxic treatment, corresponding with heightened glycolytic, lactate secretion, and gene binding ability; however, this effect diminished when HIF-1α was knocked out in PMN-MDSCs. This was evidenced by the worsened brain injury in knockout mice subjected to hypoxia, which correlated with increased microglial activation and inflammatory factor expression. The findings highlight that the HIF-1α signaling pathway related to PMN-MDSCs affects microglia activation, thereby mitigating brain injury. However, the upstream signals activating HIF-1α remain unknown and need further investigation. Additionally, while our study focused on peripheral PMN-MDSCs' effects on neonatal brain injury post-hypoxia, their regulatory roles in other tissues and organs are still unclear and require further exploration.

Lactate, a key by-product of exercise, is transported via monocarboxylate transporters (MCTs) across the BBB to various tissues, including brain regions like the hippocampus [62]. Emerging research challenges the traditional view of lactate as merely a waste product of glycolysis [61, 67], which has been reported can influence microglial phenotypic transitions and reducing neuroinflammation [63]. Additionally, lactate inhibits lipopolysaccharide (LPS)-induced neuroinflammation in mouse hippocampi [68]. In our study, we found that HIF-1α-mediated glycolysis and lactate release from PMN-MDSCs mitigate post-hypoxia brain damage in neonatal mice. Notably, lactate supplementation in hypoxic mice rescues brain damage attributed to inadequate PMN-MDSC activation owing to HIF-1α deficiency. In vitro co-culture experiments demonstrated that lactate directly influenced inflammatory factor expression in microglia. This research underscores the important role of lactate from peripheral PMN-MDSCs. Future investigations should delve deeper into how lactate facilitates transitions among microglial activation and its interplay with immune responses in the CNS. Furthermore, our study provides a novel perspective on how HIF-1α-glycolysis-mediated lactate secretion in PMN-MDSCs affects the expression of inflammatory factors in microglia. However, the mechanisms by which lactate regulates neuroinflammation warrant further investigation.

In conclusion, our study clarifies the mechanisms behind the increased activation of PMN-MDSCs in acute hypoxia and their effects on microglial activation, inflammatory factor expression in microglia, and brain injury. We also highlight the role of lactate produced by peripheral PMN-MDSCs. These findings open new research avenues for neonatal brain injury, suggesting that lactate administration may be a promising therapeutic strategy for this condition.

Limitations of the study

Our findings highlight the significant impact of peripheral PMN-MDSCs from newborns after acute hypoxia on microglia activation and inflammatory factor expression. However, the mechanisms by which these PMN-MDSCs affect specific microglial subpopulations remain unclear. Additionally, the role of lactate released by hypoxia-induced PMN-MDSCs in neuroinflammation is not fully

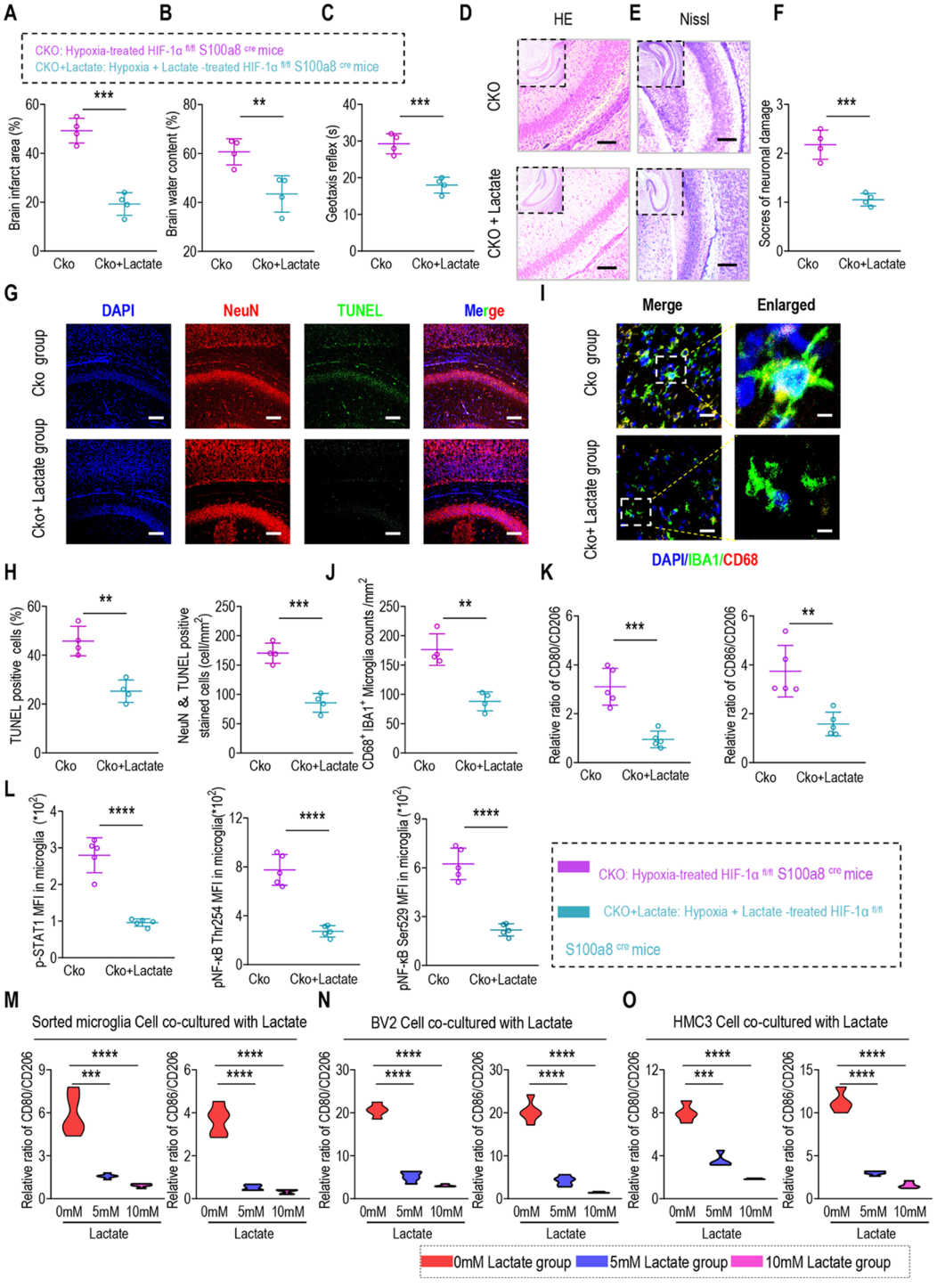

Fig. 8 (See legend on next page.)

(See figure on previous page.)

Fig. 8 Lactate from PMN-MDSCs significantly reduces brain injury by decreasing microglial activation and inflammatory factor expression. HIF-1α$^{fl/fl}$ S100A8^{cre} mice were divided into two groups: HIF-1α$^{fl/fl}$ S100A8^{cre} mice group, HIF-1α$^{fl/fl}$ S100A8^{cre} mice + Lactate group. In the intervention experiments, lactate at 2 g/kg was injected into mice intraperitoneally for two consecutive days and brain pathology was evaluated at the 48 h after hypoxia. (**A**) Statistical analysis of the percentage of brain infarct area in lactate supplementation assay ($n = 4$). (**B**) Statistical analysis of brain water content results in lactate supplementation assay ($n = 4$). (**C**) Statistical analysis of geotaxis reflex time in lactate supplementation assay ($n = 4$). (**D**) Representative H&E staining image (original magnification, ×400) in lactate supplementation assay. (**E**) Representative Nissl staining image (original magnification, ×400) and (**F**) statistical analysis of the hippocampal neuronal damage scores in lactate supplementation assay ($n = 4$). (**G**) Representative images of NeuN (red) and TUNEL staining (green) in the hippocampal region and DAPI staining is shown in blue. Scale bar = 50 μm. (**H**) Statistical analysis of the percentage of TUNEL cells and the number of NeuN-TUNEL positive mouse hippocampal neurons in lactate supplementation assay ($n = 4$). (**I** and **J**) Representative merged and enlarged images showing CD68, IBA1, and DAPI co-staining in the hippocampus (Scale bar = 50 μm) and statistical analysis of the number of CD68^{+} IBA1^{+} double positive microglia cells for lactate supplementation assay ($n = 4$). (**K**) Statistical analysis of CD80/CD206 and CD86/CD206 relative ratios after hypoxia is shown ($n = 4$). (**L**) Statistical analysis of p-STAT1, pNF-κB Thr254, and pNF-κB Ser529 levels in microglia at 48 h after hypoxia ($n = 5$). (**M-O**) Sorted microglia cell derived from neonatal mice brain or microglia cell line (BV2/HMC3 cell) was co-cultured with different concentrations lactate (5mM or 10mM). Subsequently, relative ratios of CD80/CD206 and CD86/CD206 were analyzed by flow cytometry after 72 h. Data are pooled from two independent experiments; *$P < 0.05$; **$P < 0.01$; ***$P < 0.001$; ****$P < 0.0001$. Bar graphs show the mean ± SEM. Statistical significance was determined using a two-tailed unpaired Student's *t*-test (**A-C, F, H**, and **J-O**)

understood. Under hypoxic conditions, HIF-1α evades degradation due to impaired ubiquitination, resulting in sustained elevated protein levels. The exact mechanism behind HIF-1α ubiquitination inhibition requires further investigation. Future research should aim to address these knowledge gaps and enhance our understanding of PMN-MDSCs' roles in neuroinflammation.

Abbreviations

FD	Fetal intrauterine distress
PMN-MDSCs	Polymorphonuclear myeloid-derived suppressor cells
FDNB	Fetal distress during delivery
NNB	Healthy newborns
HIE	Neonatal hypoxic ischemic encephalopathy
NSE	Neuron-specific enolase
HIBD	Hypoxic ischemic brain damage
HNB	The hypoxia model of newborn mice
CNB	Control newborn mice
CNS	Central nervous system
DAPI	4′, 6-Diamidino-2-phenylindole
PFA	Paraformaldehyde
FBS	Fetal bovine serum
PBS	Phosphate-buffered saline
ChIP	Chromatin immunoprecipitation
GO	Gene Ontology
KEGG	Kyoto Encyclopedia of Genes and Genomes
ANOVA	Analysis of variance
HIFs	Hypoxia-inducible factors
HIF-1α	Hypoxia-inducible factor-1α
HIF-1β	Aryl hydrocarbon receptor nuclear translocator
HIF-2α	Hypoxia-inducible factor-2α
ECAR	Extracellular acidification rate
OCR	Oxygen consumption rate
PBMCs	Peripheral blood mononuclear cells
ACK	Ammonium-chloride-potassium
ELISA	Enzyme-linked immunosorbent assay
RNA-seq	RNA sequencing
RT-qPCR	Real-time quantitative reverse transcription PCR
DEGs	Differentially expressed genes
GSEA	Gene Set Enrichment Analysis
KEGG	Kyoto Encyclopedia of Genes and Genomes
qPCR	Real-time quantitative PCR
ChIP	Chromatin immunoprecipitation assay
HE	Hematoxylin and eosin
PGE2	Prostaglandin E2
i.p.	Intraperitoneally
Lactate	Lactic Acid
STAT	Signal transducer and activator of transcription
NF-κB	Nuclear Factor kappa-light-chain-enhancer of activated B cells
BBB	Blood-brain barrier
IFN-γ	Interferon-γ
IL-10	Interleukin-10
IL-1β	Interleukin-1β
TGF-β	Transforming growth factor-β
S100A9	S100 Calcium Binding Protein A9
IBA1	Ionized calcium binding adaptor molecule 1
CD68	Cluster of Differentiation 68

Supplementary Information

The online version contains supplementary material available at https://doi.org/10.1186/s12974-025-03385-8.

Supplementary Material 1

Supplementary Material 2

Supplementary Material 3

Supplementary Material 4

Supplementary Material 5

Supplementary Material 6

Acknowledgements

We thank Z. Lian of the Guangdong Academy of Medical Sciences for providing the HIF-1α$^{fl/fl}$ mice. The flow cytometry used in this study was supported by the Department of Immunology at the School of Basic Medical Sciences, Southern Medical University. We express our gratitude to Editage (www.editage.cn) for providing English language editing services.

Author contributions

Y.H., Y.G., and G.Z. conceived and supervised the study, and wrote the manuscript. X.Z., L.P., S.K., T.W., W.W., S.Z., C.C., and J.Y. performed the experiments. All the authors contributed to the manuscript and approved the submitted version.

Funding

This study was supported by grants to Y. He from the National Natural Science Foundation of China (grant numbers 82171706 and 82471736), the Guangdong Basic and Applied Basic Research Foundation (grant number 2024A1515012897), and the Open Fund Project of Guangdong Academy of Medical Sciences (grant number YKY-KF202209). L. Peng received support from a grant from the Guangdong Basic and Applied Basic Research Foundation (grant number 2022A1515140172). W. Wu was funded by a grant from the Science and Technology Projects in Guangzhou (grant number 2023A04J2300).

Data availability
All data are available in the article and supplementary files, or from the corresponding authors upon reasonable request (hym0909@smu.edu.cn). RNA-seq data are available from the Sequence Read Archive (SRA) under accession number PRJNA1182531.

Declarations

Ethics approval and consent to participate
The experiments using mice were approved by the Institutional Animal Care and Use Committee of Southern Medical University (approval number: L2022022).

Competing interests
The authors declare no competing interests.

Received: 7 August 2024 / Accepted: 17 February 2025
Published online: 01 March 2025

References

1. Gravett C, Eckert LO, Gravett MG, Dudley DJ, Stringer EM, Mujobu TB, Lyabis O, Kochhar S, Swamy GK. Non-reassuring fetal status: case definition & guidelines for data collection, analysis, and presentation of immunization safety data. Vaccine. 2016;34:6084–92.
2. Zhang Y, Deng Y, Zhou Z, Zhang X, Jiao P, Zhao Z. Multimodal learning for fetal distress diagnosis using a multimodal medical information fusion framework. Front Physiol. 2022;13:1021400.
3. Seitz M, Köster C, Dzietko M, Sabir H, Serdar M, Felderhoff-Müser U, Bendix I, Herz J. Hypothermia modulates myeloid cell polarization in neonatal hypoxic-ischemic brain injury. J Neuroinflammation. 2021;18:266.
4. Rao R, Mietzsch U, DiGeronimo R, Hamrick SE, Dizon MLV, Lee KS, Natarajan G, Yanowitz TD, Peeples ES, Flibotte J, et al. Utilization of therapeutic hypothermia and neurological injury in neonates with mild Hypoxic-Ischemic encephalopathy: A report from children's hospital neonatal consortium. Am J Perinatol. 2022;39:319–28.
5. Herz J, Köster C, Reinboth BS, Dzietko M, Hansen W, Sabir H, van Velthoven C, Bendix I, Felderhoff-Müser U. Interaction between hypothermia and delayed mesenchymal stem cell therapy in neonatal hypoxic-ischemic brain injury. Brain Behav Immun. 2018;70:118–30.
6. Ammerdorffer A, McDougall ARA, Tuttle A, Rushwan S, Chinery L, Vogel JP, Goldstein M, Gülmezoglu AM. The drug drought in maternal health: an ongoing predicament. Lancet Glob Health. 2024;12:e1174–83.
7. Jiang L, Chen Y, Wang Q, Wang X, Luo X, Chen J, Han H, Sun Y, Shen H. A Chinese practice guideline of the assisted reproductive technology strategies for women with advanced age. J Evid Based Med. 2019;12:167–84.
8. Xiong L, Ye X, Chen Z, Fu H, Li S, Xu P, Yu J, Wen L, Gao R, Fu Y, et al. Advanced maternal Age-associated SIRT1 deficiency compromises trophoblast Epithelial-Mesenchymal transition through an increase in vimentin acetylation. Aging Cell. 2021;20:e13491.
9. Ludford I, Scheil W, Tucker G, Grivell R. Pregnancy outcomes for nulliparous women of advanced maternal age in South Australia, 1998–2008. Aust N Z J Obstet Gynaecol. 2012;52:235–41.
10. Salter MW, Stevens B. Microglia emerge as central players in brain disease. Nat Med. 2017;23:1018–27.
11. Ronzano R, Roux T, Thetiot M, Aigrot MS, Richard L, Lejeune FX, Mazuir E, Vallat JM, Lubetzki C, Desmazières A. Microglia-neuron interaction at nodes of Ranvier depends on neuronal activity through potassium release and contributes to remyelination. Nat Commun. 2021;12:5219.
12. Hickman S, Izzy S, Sen P, Morsett L, El Khoury J. Microglia in neurodegeneration. Nat Neurosci. 2018;21:1359–69.
13. Khan F, Pang L, Dunterman M, Lesniak MS, Heimberger AB, Chen P. Macrophages and microglia in glioblastoma: heterogeneity, plasticity, and therapy. J Clin Invest;2023:133.
14. McGill BE, Barve RA, Maloney SE, Strickland A, Rensing N, Wang PL, Wong M, Head R, Wozniak DF, Milbrandt J. Abnormal microglia and enhanced Inflammation-Related gene transcription in mice with conditional deletion of Ctcf in Camk2a-Cre-Expressing neurons. J Neurosci. 2018;38:200–19.
15. Wu Y, Dong JH, Dai YF, Zhu MZ, Wang MY, Zhang Y, Pan YD, Yuan XR, Guo ZX, Wang CX, et al. Hepatic soluble epoxide hydrolase activity regulates cerebral Aβ metabolism and the pathogenesis of Alzheimer's disease in mice. Neuron. 2023;111:2847–e28622810.
16. Zhang W, Han Y, Huang H, Su Y, Ren H, Qi C, Li J, Yang H, Xu J, Chang G, et al. CD22 Blockade exacerbates neuroinflammation in neuromyelitis Optica spectrum disorder. J Neuroinflammation. 2024;21:313.
17. Nassrallah WB, Li HR, Irani L, Wijesinghe P, Hogg PW, Hui L, Oh J, Mackenzie IR, Hirsch-Reinshagen V, Hsiung GR, et al. 3-Dimensional morphological characterization of neuroretinal microglia in Alzheimer's disease via machine learning. Acta Neuropathol Commun. 2024;12:202.
18. Müller A, Brandenburg S, Turkowski K, Müller S, Vajkoczy P. Resident microglia, and not peripheral macrophages, are the main source of brain tumor mononuclear cells. Int J Cancer. 2015;137:278–88.
19. Jurga AM, Paleczna M, Kuter KZ. Overview of general and discriminating markers of differential microglia phenotypes. Front Cell Neurosci. 2020;14:198.
20. Pombo Antunes AR, Scheyltjens I, Lodi F, Messiaen J, Antoranz A, Duerinck J, Kancheva D, Martens L, De Vlaminck K, Van Hove H, et al. Single-cell profiling of myeloid cells in glioblastoma across species and disease stage reveals macrophage competition and specialization. Nat Neurosci. 2021;24:595–610.
21. Yang X, Xu S, Qian Y, Xiao Q. Resveratrol regulates microglia M1/M2 polarization via PGC-1α in conditions of neuroinflammatory injury. Brain Behav Immun. 2017;64:162–72.
22. Prichard A, Garza KM, Shridhar A, He C, Bitarafan S, Pybus A, Wang Y, Snyder E, Goodson MC, Franklin TC, et al. Brain rhythms control microglial response and cytokine expression via NF-κB signaling. Sci Adv. 2023;9:eadf5672.
23. Oliynyk Z, Rudyk M, Dovbynchuk T, Dzubenko N, Tolstanova G, Skivka L. Inflammatory hallmarks in 6-OHDA- and LPS-induced Parkinson's disease in rats. Brain Behav Immun Health. 2023;30:100616.
24. He YM, Li X, Perego M, Nefedova Y, Kossenkov AV, Jensen EA, Kagan V, Liu YF, Fu SY, Ye QJ, et al. Transitory presence of myeloid-derived suppressor cells in neonates is critical for control of inflammation. Nat Med. 2018;24:224–31.
25. Cui Z, Xu H, Wu F, Chen J, Zhu L, Shen Z, Yi X, Yang J, Jia C, Zhang L, et al. Maternal circadian rhythm disruption affects neonatal inflammation via metabolic reprograming of myeloid cells. Nat Metab. 2024;6:899–913.
26. Vance JK, Rawson TW, Povroznik JM, Brundage KM, Robinson CM. Myeloid-Derived suppressor cells gain suppressive function during neonatal bacterial Sepsis. Int J Mol Sci. 2021;22.
27. Fan X, Heijnen CJ, van der Kooij MA, Groenendaal F, van Bel F. The role and regulation of hypoxia-inducible factor-1alpha expression in brain development and neonatal hypoxic-ischemic brain injury. Brain Res Rev. 2009;62:99–108.
28. Sun L. F-box and WD repeat domain-containing 7 (FBXW7) mediates the hypoxia inducible factor-1α (HIF-1α)/vascular endothelial growth factor (VEGF) signaling pathway to affect hypoxic-ischemic brain damage in neonatal rats. Bioengineered. 2022;13:560–72.
29. Kunze R, Zhou W, Veltkamp R, Wielockx B, Breier G, Marti HH. Neuron-specific prolyl-4-hydroxylase domain 2 knockout reduces brain injury after transient cerebral ischemia. Stroke. 2012;43:2748–56.
30. Chen RL, Nagel S, Papadakis M, Bishop T, Pollard P, Ratcliffe PJ, Pugh CW, Buchan AM. Roles of individual prolyl-4-hydroxylase isoforms in the first 24 hours following transient focal cerebral ischaemia: insights from genetically modified mice. J Physiol. 2012;590:4079–91.
31. Helton R, Cui J, Scheel JR, Ellison JA, Ames C, Gibson C, Blouw B, Ouyang L, Dragatsis I, Zeitlin S, et al. Brain-specific knock-out of hypoxia-inducible factor-1alpha reduces rather than increases hypoxic-ischemic damage. J Neurosci. 2005;25:4099–107.
32. Kuan CY, Chen HR, Gao N, Kuo YM, Chen CW, Yang D, Kinkaid MM, Hu E, Sun YY. Brain-targeted hypoxia-inducible factor stabilization reduces neonatal hypoxic-ischemic brain injury. Neurobiol Dis. 2021;148:105200.
33. Ogle ME, Gu X, Espinera AR, Wei L. Inhibition of Prolyl hydroxylases by dimethyloxaloylglycine after stroke reduces ischemic brain injury and requires hypoxia inducible factor-1α. Neurobiol Dis. 2012;45:733–42.
34. Chen RL, Ogunshola OO, Yeoh KK, Jani A, Papadakis M, Nagel S, Schofield CJ, Buchan AM. HIF Prolyl hydroxylase Inhibition prior to transient focal cerebral ischaemia is neuroprotective in mice. J Neurochem. 2014;131:177–89.
35. Liu G, Bi Y, Shen B, Yang H, Zhang Y, Wang X, Liu H, Lu Y, Liao J, Chen X, Chu Y. SIRT1 limits the function and fate of myeloid-derived suppressor cells in tumors by orchestrating HIF-1α-dependent Glycolysis. Cancer Res. 2014;74:727–37.
36. Zhang Z, Zheng Y, Chen Y, Yin Y, Chen Y, Chen Q, Hou Y, Shen S, Lv M, Wang T. Gut fungi enhances immunosuppressive function of myeloid-derived

suppressor cells by activating PKM2-dependent Glycolysis to promote colorectal tumorigenesis. Exp Hematol Oncol. 2022;11:88.
37. Chen X, Zhang Z, Bi Y, Fu Z, Gong P, Li Y, Yu Q, Jia A, Wang J, Xue L, et al. mTOR signaling disruption from myeloid-derived suppressive cells protects against immune-mediated hepatic injury through the HIF1α-dependent glycolytic pathway. J Leukoc Biol. 2016;100:1349–62.
38. Horn CM, Arumugam P, Van Roy Z, Heim CE, Fallet RW, Bertrand BP, Shinde D, Thomas VC, Romanova SG, Bronich TK et al. Granulocytic myeloid-derived suppressor cell activity during biofilm infection is regulated by a glycolysis/HIF1a axis. J Clin Invest. 2024;134.
39. Jian SL, Chen WW, Su YC, Su YW, Chuang TH, Hsu SC, Huang LR. Glycolysis regulates the expansion of myeloid-derived suppressor cells in tumor-bearing hosts through prevention of ROS-mediated apoptosis. Cell Death Dis. 2017;8:e2779.
40. Ou X, Lv W. Metabolic changes and interaction of tumor cell, myeloid-derived suppressor cell and T cell in hypoxic microenvironment. Future Oncol. 2020;16:383–93.
41. Bertrand BP, Heim CE, Koepsell SA, Kielian T. Elucidating granulocytic myeloid-derived suppressor cell heterogeneity during Staphylococcus aureus biofilm infection. J Leukoc Biol. 2024;115:620–32.
42. Lu Y, Liu H, Bi Y, Yang H, Li Y, Wang J, Zhang Z, Wang Y, Li C, Jia A, et al. Glucocorticoid receptor promotes the function of myeloid-derived suppressor cells by suppressing HIF1α-dependent Glycolysis. Cell Mol Immunol. 2018;15:618–29.
43. Li X, Liu J, Xing Z, Tang J, Sun H, Zhang X, Lv S, Chen Z, Shi M, Chen M, et al. Polymorphonuclear myeloid-derived suppressor cells link inflammation and damage response after trauma. J Leukoc Biol. 2021;110:1143–61.
44. Wu H, Zheng J, Xu S, Fang Y, Wu Y, Zeng J, Shao A, Shi L, Lu J, Mei S, et al. Mer regulates microglial/macrophage M1/M2 polarization and alleviates neuroinflammation following traumatic brain injury. J Neuroinflammation. 2021;18:2.
45. Shi M, Chen Z, Chen M, Liu J, Li J, Xing Z, Zhang X, Lv S, Li X, Zuo S, et al. Continuous activation of polymorphonuclear myeloid-derived suppressor cells during pregnancy is critical for fetal development. Cell Mol Immunol. 2021;18:1692–707.
46. Chen J, Jin J, Zhang X, Yu H, Zhu X, Yu L, Chen Y, Liu P, Dong X, Cao X, et al. Microglial lnc-U90926 facilitates neutrophil infiltration in ischemic stroke via MDH2/CXCL2 axis. Mol Ther. 2021;29:2873–85.
47. Jiang D, Zhao J, Zheng J, Zhao Y, Le M, Qin D, Huang Q, Huang J, Zhao Q, Wang L, Dong X. LOX-mediated ECM mechanical stress induces Piezo1 activation in hypoxic-ischemic brain damage and identification of novel inhibitor of LOX. Redox Biol. 2024;76:103346.
48. Chen Y, Fang X, Liu H, Fan Q. Knockdown of IGF2BP3 Down-Regulates PDCD4 levels to attenuate Hypoxic-Ischemic brain damage. Front Biosci (Landmark Ed). 2024;29:329.
49. Kumar AJ, Motta-Teixeira LC, Takada SH, Yonamine-Lee V, Machado-Nils AV, Xavier GF, Nogueira MI. Behavioral, cognitive and histological changes following neonatal anoxia: male and female rats' differences at adolescent age. Int J Dev Neurosci. 2019;73:50–8.
50. Takada SH, Dos Santos Haemmerle CA, Motta-Teixeira LC, Machado-Nils AV, Lee VY, Takase LF, Cruz-Rizzolo RJ, Kihara AH, Xavier GF, Watanabe IS, Nogueira MI. Neonatal anoxia in rats: hippocampal cellular and subcellular changes related to cell death and Spatial memory. Neuroscience. 2015;284:247–59.
51. Fu Q, Wu J, Zhou XY, Ji MH, Mao QH, Li Q, Zong MM, Zhou ZQ, Yang JJ. NLRP3/Caspase-1 Pathway-Induced pyroptosis mediated cognitive deficits in a mouse model of Sepsis-Associated encephalopathy. Inflammation. 2019;42:306–18.
52. Liu YS, Wang ML, Hu NY, Li ZM, Wu JL, Li H, Li JT, Li XW, Yang JM, Gao TM, Chen YH. A comparison of the impact on neuronal transcriptome and cognition of rAAV5 transduction with three different doses in the mouse hippocampus. Front Mol Neurosci. 2023;16:1195327.
53. Hung TH, Liu YC, Wu CH, Chen CC, Chao H, Yang FY, Chen SF. Antenatal low-intensity pulsed ultrasound reduces neurobehavioral deficits and brain injury following dexamethasone-induced intrauterine growth restriction. Brain Pathol. 2021;31:e12968.
54. Zhang X, Liu J, Li X, Zheng G, Wang T, Sun H, Huang Z, He J, Qiu J, Zhao Z et al. Blocking the HIF-1α/glycolysis axis inhibits allergic airway inflammation by reducing ILC2 metabolism and function. Allergy. 2024.
55. Lv S, Chen M, Li Z, Huang Z, Wan S, Kuang S, Peng L, Ye J, Yang M, Li J, He Y. Blocking OLFM4/galectin-3 axis in placental polymorphonuclear myeloid-derived suppressor cells triggers intestinal inflammation in newborns. Int Immunopharmacol. 2024;133:112058.
56. Pu F, Chen F, Zhang Z, Shi D, Zhong B, Lv X, Tucker AB, Fan J, Li AJ, Qin K, et al. Ferroptosis as a novel form of regulated cell death: implications in the pathogenesis, oncometabolism and treatment of human cancer. Genes Dis. 2022;9:347–57.
57. Liu Y, Perego M, Xiao Q, He Y, Fu S, He J, Liu W, Li X, Tang Y, Li X, et al. Lactoferrin-induced myeloid-derived suppressor cell therapy attenuates pathologic inflammatory conditions in newborn mice. J Clin Invest. 2019;129:4261–75.
58. Liu H, Liao J, Jiang Y, Zhang B, Yu H, Kang J, Hu C, Li Y, Xu S. Maternal exposure to fine particulate matter and the risk of fetal distress. Ecotoxicol Environ Saf. 2019;170:253–8.
59. Chen R, Lin Z, Shen S, Zhu C, Yan K, Suo C, Liu R, Wei H, Gao L, Fan K, et al. Citrullination modulation stabilizes HIF-1α to promote tumour progression. Nat Commun. 2024;15:7654.
60. Chen Y, Xu X, Wang Y, Zhang Y, Zhou T, Jiang W, Wang Z, Chang J, Liu S, Chen R, et al. Hypoxia-induced SKA3 promoted cholangiocarcinoma progression and chemoresistance by enhancing fatty acid synthesis via the regulation of PAR-dependent HIF-1a deubiquitylation. J Exp Clin Cancer Res. 2023;42:265.
61. Magistretti PJ, Allaman I. Lactate in the brain: from metabolic end-product to signalling molecule. Nat Rev Neurosci. 2018;19:235–49.
62. Morland C, Andersson KA, Haugen ØP, Hadzic A, Kleppa L, Gille A, Rinholm JE, Palibrk V, Diget EH, Kennedy LH, et al. Exercise induces cerebral VEGF and angiogenesis via the lactate receptor HCAR1. Nat Commun. 2017;8:15557.
63. Han H, Zhao Y, Du J, Wang S, Yang X, Li W, Song J, Zhang S, Zhang Z, Tan Y, et al. Exercise improves cognitive dysfunction and neuroinflammation in mice through histone H3 lactylation in microglia. Immun Ageing. 2023;20:63.
64. Sanmarco LM, Rone JM, Polonio CM, Fernandez Lahore G, Giovannoni F, Ferrara K, Gutierrez-Vazquez C, Li N, Sokolovska A, Plasencia A, et al. Lactate limits CNS autoimmunity by stabilizing HIF-1α in dendritic cells. Nature. 2023;620:881–9.
65. Qian Y, Galan-Cobo A, Guijarro I, Dang M, Molkentine D, Poteete A, Zhang F, Wang Q, Wang J, Parra E, et al. MCT4-dependent lactate secretion suppresses antitumor immunity in LKB1-deficient lung adenocarcinoma. Cancer Cell. 2023;41:1363–e13801367.
66. Hu X, Li P, Guo Y, Wang H, Leak RK, Chen S, Gao Y, Chen J. Microglia/macrophage polarization dynamics reveal novel mechanism of injury expansion after focal cerebral ischemia. Stroke. 2012;43:3063–70.
67. Rinholm JE, Hamilton NB, Kessaris N, Richardson WD, Bergersen LH, Attwell D. Regulation of oligodendrocyte development and myelination by glucose and lactate. J Neurosci. 2011;31:538–48.
68. Liang L, Liu P, Deng Y, Li J, Zhao S. L- lactate inhibits lipopolysaccharide-induced inflammation of microglia in the hippocampus. Int J Neurosci. 2024;134:45–52.

Publisher's note